

Chemotactic NO/H₂S Nanomotors Realizing Cardiac Targeting of G-CSF against Myocardial Ischemia-Reperfusion Injury

Nan Li,[¶] Chenxing Huang,[¶] Jie Zhang,[¶] Junyue Zhang, Jia Huang, Shangshang Li, Xue Xia, Ziyu Wu, Chenglong Chen, Shuwan Tang, Xiangyu Xiao, Hui Gong, Yuxiang Dai,^{*} Chun Mao,^{*} and Mimi Wan^{*}

Cite This: <https://doi.org/10.1021/acsnano.3c02781>

Read Online

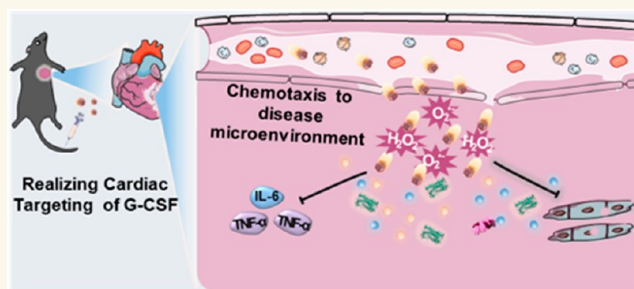
ACCESS |

Metrics & More

Article Recommendations

Supporting Information

ABSTRACT: Recombinant granulocyte colony-stimulating factor (G-CSF), with a direct repair effect on injured cardiomyocytes against myocardial infarction ischemia-reperfusion-injury (IRI), displays a poor effect owing to the limited cardiac targeting efficacy. There are almost no reports of nanomaterials that deliver G-CSF to the IRI site. Herein, we propose a way to protect G-CSF by constructing one layer of nitric oxide (NO)/hydrogen sulfide (H₂S) nanomotors on its outside. NO/H₂S nanomotors with specific chemotactic ability to high expression of reactive oxygen species (ROS)/induced nitric oxide synthase (iNOS) at the IRI site can deliver G-CSF to the IRI site efficiently. Meanwhile, superoxide dismutase is covalently bound to the outermost part, reducing ROS at the IRI site through a cascade effect with NO/H₂S nanomotors. The synergistic effect between NO and H₂S on the effective regulation of the IRI microenvironment can not only avoid toxicity caused by excessive concentration of a single gas but also reduce inflammation level and relieve calcium overload, so as to promote G-CSF to play a cardioprotective role.



KEYWORDS: ischemia-reperfusion injury, nanomotors, nitric oxide, hydrogen sulfide, targeted delivery

INTRODUCTION

Ischemia-reperfusion (IR) is currently one of the most important clinical treatments for myocardial infarction.^{1,2} However, during reperfusion, the influx of oxygen prompts the reactivation of the electron transport chain of aerobic metabolism and the overproduction of reactive oxygen species (ROS), and inducible nitric oxide synthase (iNOS, not expressed in normal cells),^{3–6} which disrupts the dynamic balance between endogenous pro- and antioxidant functions, resulting in a significant increase in oxidative stress in the body.^{7,8} Oxidative stress then induces a pro-inflammatory immune cascade response, i.e., infiltration of inflammatory cells, release of inflammatory mediators, and ultimately myocardial cell damage and death.^{9–11} In addition, this process is accompanied by Ca²⁺ overload due to ion pump failure, which causes additional damage to cardiomyocytes.^{12–14} Therefore, ischemia-reperfusion injury (IRI) in myocardial infarction is a challenging problem that must be faced after IR treatment. And effective elimination of ROS and the inflammatory response within 48 h of reperfusion to prevent cardiomyocyte apoptosis and necrosis triggered by the

inflammatory storm is considered key to interrupting the vicious cycle caused by IRI.^{15–18}

Pharmacological intervention at the onset of reperfusion is one of the most clinically feasible therapeutic approaches available.^{10,19} Examples include statins, which stabilize atherosclerotic plaques by lowering blood lipids to slow deterioration, and β -blockers, which prolong cardiomyocyte activity by reducing energy consumption.^{20–23} However, these drugs only target the deterioration that has already occurred, and they do not have a direct effect on cardiomyocytes, making it difficult to prevent the continuation of deterioration and achieve effective cardiomyocyte repair. Recombinant granulocyte colony-stimulating factor (G-CSF) has been shown to protect injured cardiomyocytes by directly upregulating antiapoptotic proteins in cardiomyocytes, reducing infarct

Received: March 27, 2023

Accepted: June 13, 2023

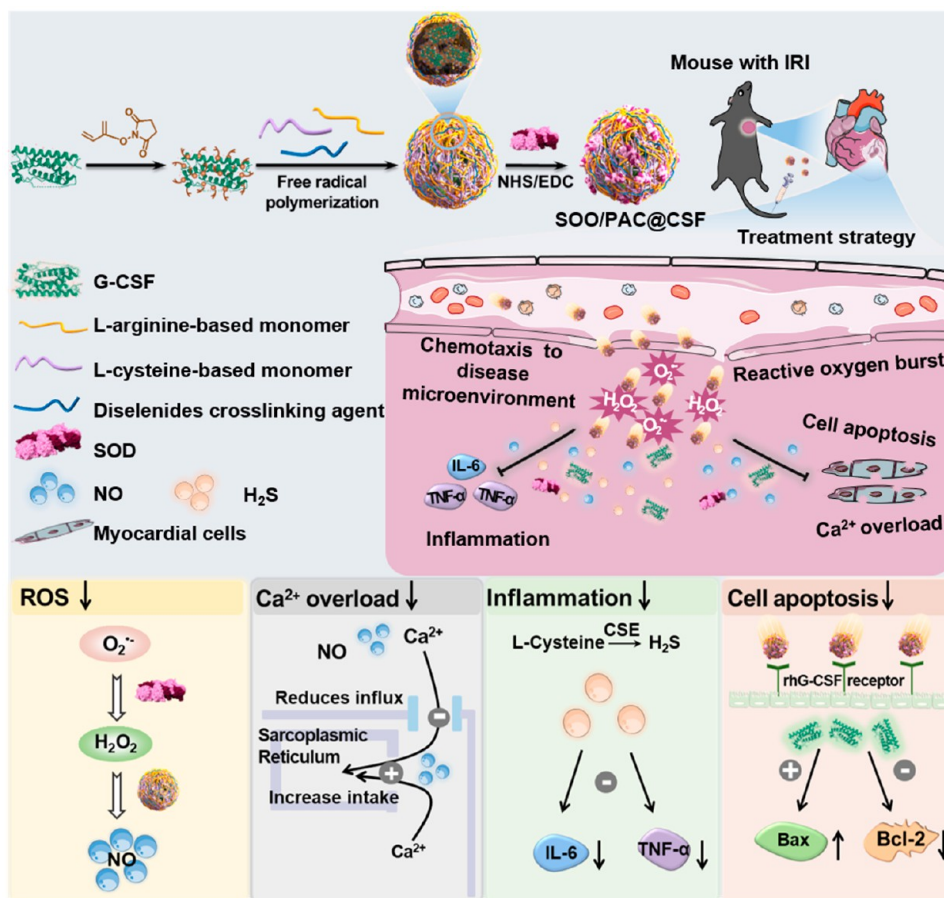


Figure 1. Schematic illustrating the fabrication of NO/H₂S SOD/PAC@CSF nanomotors and their chemotaxis to the disease microenvironment, responsive drug release, and treatment of IRI.

size and thus gaining increasing clinical attention.^{24–26} However, given that G-CSF must reach the site of cardiac injury to be effective and that in clinical practice it is usually administered systemically by subcutaneous or intravenous injection, very high doses are required to achieve effective therapeutic concentrations in the IRI region. But systemic administration of high doses of G-CSF has potential toxicity issues (causing elevated neutrophil concentrations) that severely limit its therapeutic potential.^{27,28} Meanwhile, the highly inflammatory environment caused by the presence of large amounts of ROS in the IRI microenvironment may also hinder the effect of G-CSF due to microvascular occlusion caused by inflammatory cell aggregation, which is another important factor limiting its clinical efficacy.^{8,9,29,30} Therefore, there is an urgent need to design and develop effective strategies that can improve the efficiency of G-CSF cardiac targeting and retention and effectively modulate the inflammatory microenvironment of the IRI to improve the therapeutic efficacy of G-CSF.

In recent years, a variety of nanocarriers have been introduced to deliver G-CSF, such as the use of polymeric materials or bioderived exosomes to increase the half-life and stability of G-CSF *in vivo*, and the use of calcium carbonate and dextran nanoparticles to slowly release G-CSF for the treatment of neutropenia, leukemia, cancer, and other diseases to improve the bioavailability of G-CSF to some extent.^{31–34} However, the specific location of the heart, with its systolic–diastolic dynamic activity accompanied by large changes in

ventricular volume, triggers rapid and massive blood exchange, making it difficult for the drug to remain in the heart for long periods of time and much more difficult to accumulate at the site of IRI.³⁵ Therefore, the above-mentioned delivery system for G-CSF cannot be directly applied to the treatment of IRI, and there is still a great challenge to develop a delivery system that can effectively achieve the effective aggregation of G-CSF at the site of IRI.

The typical character of the high ROS and iNOS microenvironment of IRI provides an idea for achieving precise targeting to the site of cardiac injury. Accordingly, the NO/H₂S nanomotors were designed and constructed using *N*-methacryl-L-arginine (M-Arg) and *N*-methacryloyl-L-cysteine (M-Cys) as monomers, respectively, and a polymeric shell layer wrapped around the outside of G-CSF by a radical polymerization reaction under reaction with a degradable cross-linking agent (Figure 1). The M-Arg and M-Cys components of the shell layer react with ROS/iNOS and cystathionine gamma-lyase (CSE) present in the IRI microenvironment to produce nitric oxide (NO) and hydrogen sulfide (H₂S),^{36–38} respectively, forming the NO/H₂S nanomotors. Subsequently, superoxide dismutase (SOD) is covalently cross-linked in the polymer shell layer to convert the surplus O₂^{•-} at the IRI site into H₂O₂,¹⁷ which can be further consumed by the nanomotors to yield NO, constituting a cascade effect that both converts ROS into nontoxic components and increases the motion efficiency of the nanomotors.

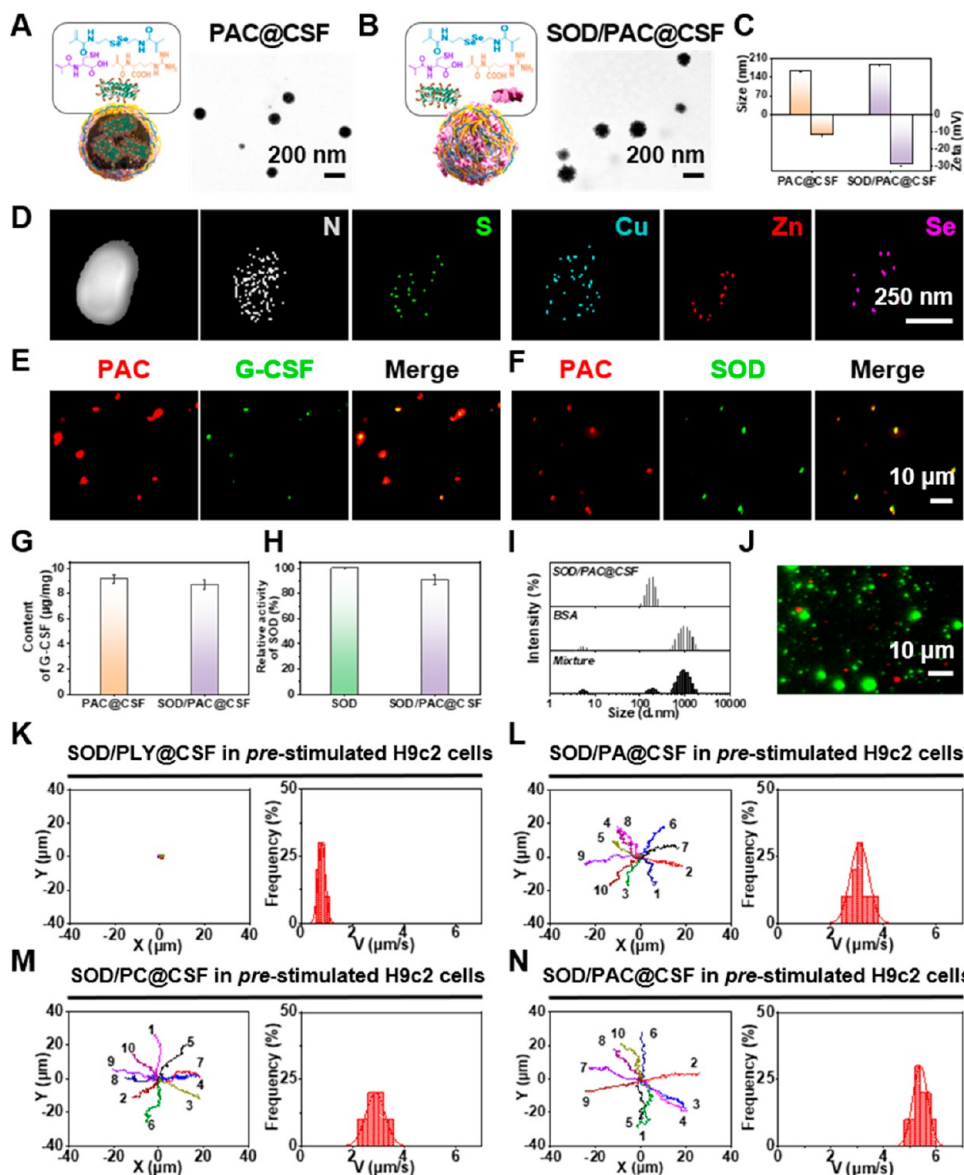


Figure 2. Characterizations of different samples. TEM images of (A) PAC@CSF, (B) SOD/PAC@CSF. (C) DLS results and zeta potential analysis of PAC@CSF and SOD/PAC@CSF. (D) High angle annular dark field STEM and corresponding TEM-mapping of SOD/PAC@CSF. Fluorescence image of (E) PAC (labeled with cy5-NH₂, red) @CSF (labeled with FITC, green) and (F) SOD (labeled with FITC, green)/PAC (labeled with cy5-NH₂, red). (G) Content of G-CSF in PAC@CSF and SOD/PAC@CSF. (H) Relative enzyme activity of pure SOD and SOD/PAC@CSF. (I) DLS result analysis of SOD/PAC@CSF (1 mg mL⁻¹) and BSA (500 mg mL⁻¹) after incubation at 37 °C for 4 h. (J) Fluorescence image of the mixed solution of cy5-NH₂ labeled SOD/PAC@CSF (1 mg mL⁻¹, red) and FITC-labeled BSA (500 mg mL⁻¹, green) after incubation at 37 °C for 4 h (the image was taken after the solution was diluted 1000 times). Trajectory and velocity distribution of (K) SOD/PLY@CSF, (L) SOD/PA@CSF, (M) SOD/PC@CSF, and (N) SOD/PAC@CSF in prestimulated H9c2 cells (20 s, $n = 10$). Experimental data are means \pm SD of samples in a representative experiment ($n = 3$). * $P < 0.05$, ** $P < 0.01$, and *** $P < 0.001$, determined by one-way analysis of variance (ANOVA).

The nanomotors can use the specific affinity interaction (enzyme–substrate interaction) between the M-Arg in its component and the highly expressed iNOS in the IRI microenvironment to form a chemotactic effect to the IRI site, enabling effective targeting and retention in the IRI area.³⁸ The nanomotors retained at the IRI site can effectively eliminate the high levels of ROS already present by exploiting the cascade effect between the SOD and M-Arg in their components. The generated H₂S can also reduce the further expression of ROS by stimulating the activity of glutathione (GSH) and thioredoxin,^{39–41} thus reducing the overall inflammatory level, and NO can also relieve calcium overload

by inhibiting the opening of L-type Ca²⁺ channels, increasing the activity of ATP-sensitive potassium (K_{ATP}) channels and increasing the activity of sarcoplasmic reticulum Ca²⁺-ATPase (SERCA).^{42,43} This process is accompanied by the degradation of the polymer shell and the release of G-CSF, and this multifaceted, multilinked approach to regulating the inflammatory microenvironment will facilitate the better function of G-CSF in myocardial repair, leading to the effective treatment of IRI. In particular, the two gas concepts proposed in this work can prevent the toxicity caused by high local concentration of a certain gas while maintaining sufficient driving force for the nanomotors.

RESULTS

Characterization of the Nanomotors. According to the previous method,^{44–47} to prepare polymer monomer, L-arginine and L-cysteine were conjugated with methacrylate anhydride and methyl acrylyl chloride, respectively, to form N-methacryl-L-arginine (M-Arg) and N-methacryloyl-L-cysteine (M-Cys) containing a carbon–carbon double bond. The diselenide cross-linker responsive to ROS degradation synthesized by an amidation reactions.⁴⁸ Then, M-Arg and M-Cys can act as monomer to react with diselenide cross-linker to form polymer shell (PAC) on the outside of CSF to give PAC@CSF. The structures of above precursors including M-Arg, M-Cys and diselenide were characterized by ¹H NMR (Figure S1, S2, and S3). Next, SOD was modified on the surface of PAC@CSF by weak covalent bonding to obtain the NO/H₂S SOD/PAC@CSF. As observed from the transmission electron microscopy (TEM) images (Figure 2A and B) and dynamic light scattering (DLS) results (Figure 2C), PAC@CSF and SOD/PAC@CSF are spherulike and their diameters are comparable to the DLS results, which increased from 163.2 to about 186.5 nm after loading SOD. Zeta potential analysis of different samples showed that the negative charge of PAC@CSF increased significantly (from −12.0 to −29.0 mV) after SOD loading when the abundant carboxylic acid groups in PAC@CSF combined with the amino groups in SOD, which may be due to the negative charge carried by SOD increasing the negative surface charge of SOD/PAC@CSF (Figure 2C). Also, we recorded the hydrodynamic diameters of SOD/PAC@CSF nanomotors after 48 h of dispersion in phosphate buffered solution (PBS), serum solution (10% fetal bovine serum), and Dulbecco's modified Eagle's medium, as shown in Figure S4. The slight changes in hydrodynamic dimensions indicate the good stability of the SOD/PAC@CSF nanomotors. We also use TEM-mapping to characterize the presence of N, S, Cu/Zn, and Se in the final product (Figure 2D). To visualize the presence of different components in SOD/PAC@CSF, PAC-Cy5@CSF-FITC nanomotors were also prepared by integrating cy5-labeled PAC (red) and FITC-labeled G-CSF (green). The merged fluorescence of red PAC and green G-CSF when observed by confocal laser scanning microscopy (CLSM) further confirms the successful preparation of SOD/PAC@CSF (Figure 2E). Similarly, when SOD was labeled with FITC, the green fluorescence representing SOD and the red fluorescence representing PAC also overlapped well, indicating that SOD can successfully combine with PAC (Figure 2F). The binding content of G-CSF in PAC@CSF and SOD/PAC@CSF (Figure 2G) was determined by antigen–antibody assay, which was 9.2 μg mg^{−1} and 8.7 μg mg^{−1}, respectively. At the same time, it can be inferred that the encapsulation efficiency of G-CSF remained above 87.2% (Figure S5). Similarly, compared to free SOD, SOD on SOD/PAC@CSF retained more than 91.7% of the enzyme activity, indicating good efficacy retention of the covalently bound enzyme (Figure 2H).

Then, the degradation capability of SOD/PAC@CSF was evaluated. As shown in Figure S6 the relative turbidity of the system is dramatically reduced within 12 h, which can be attributed to the presence of diselenide cross-linker, which can respond to the ROS to degrade. In addition, the zwitterion-based nanomotors SOD/PAC@CSF possesses an antiprotein adhesion function. After 4 h of mixing the nanomotors with bovine serum albumin (BSA), the mixed solution exhibited

typical peaks (Figure 2I), which may represent the particle size of SOD/PAC@CSF (190.1 nm) and bovine serum albumin (5.6 and 955.4 nm). Fluorescence images also show that there is no overlap between the red fluorescence on the nanomotors and the green fluorescence of BSA (Figure 2J), illustrating that BSA NPs are not adsorbed on the nanomotors. This antiprotein adhesion property facilitates prolonged *in vivo* circulation, while the ROS responsiveness ensures the stability of nanomotors in the *in vivo* circulation (ROS-poor site) and the release of the cargoes in at the ROS-rich target site.

The typical character of the microenvironment caused by IRI is the high-level ROS and the high expression iNOS. SOD and M-Arg in SOD/PAC@CSF nanomotors can reduce a high level of ROS through a cascade effect. At the IRI site, SOD can reduce a large amount of O₂^{•−} into H₂O₂, and then M-Arg can react with H₂O₂ or be catalyzed by highly expressed iNOS to generate NO, while M-Cys can be catalyzed by CSE to generate H₂S, thus forming a NO/H₂S nanomotors. For comparison, non-nanomotor SOD/PLY@CSF NPs (with N-methacryl-L-lysine, M-Lys, as monomer), NO SOD/PA@CSF nanomotors (with M-Arg as monomer), and H₂S SOD/PC@CSF nanomotors (with M-Cys as monomer) were also prepared by similar synthetic methods. The particle size results for the above materials were similar to those of the SOD/PAC@CSF nanomotors, corresponding to 180.2, 175.5, and 179.0 nm (Figure S7). Among them, the synthesized M-Lys from L-lysine and methacrylate anhydride, which replaced M-Arg and M-Cys as substrates for the synthesis of SOD/PLY@CSF NPs, was also characterized, and its presence was confirmed by ¹H NMR (Figure S8).

Then, the movement behaviors of non-nanomotor SOD/PLY@CSF NPs, NO SOD/PA@CSF nanomotors, and H₂S SOD/PC@CSF nanomotors were investigated in the H9c2 cell environment. In normal H9c2 cells, the SOD/PLY@CSF NPs, SOD/PA@CSF, SOD/PC@CSF, and SOD/PAC@CSF nanomotors all show distinct Brownian motion trajectories and velocity distributions (less than 1.0 μm s^{−1}) (Figure S9, Movie S1–S4), which may be attributed to the low ROS levels. When H9c2 cells were prestimulated with lipopolysaccharide (LPS), a stimulator for inducing cellular inflammatory injury) for 24 h,^{49,50} noticeable trajectory toward different directions and boosted velocity distributions were observed on SOD/PA@CSF, SOD/PC@CSF, and SOD/PAC@CSF nanomotors, while SOD/PLY@CSF NPs remained in Brownian motion (Figure 2K–N, Movie S5–S8). Compared to SOD/PAC@CSF with a velocity of 5.4 μm s^{−1}, SOD/PA@CSF (3.1 μm s^{−1}) and SOD/PC@CSF (2.9 μm s^{−1}) show relatively slower velocity, demonstrating the higher motion potential of the NO/H₂S nanomotors. Also, the motility of the SOD/PAC@CSF nanomotors was examined after coinubation with prestimulated H9c2 cells for different times to assess the lifetime of the nanomotors (Figure S10, Movie S9). It can be seen that the average speed of the nanomotors decreased slightly over time from ~5.4 μm s^{−1} (0 h) to ~4.2 μm s^{−1} (24 h) while maintaining 77.8% of the speed, indicating that the lifetime of the SOD/PAC@CSF nanomotors can be essentially maintained for 24 h.

After that, the release of NO and H₂S from H9c2 cells was evaluated, and H9c2 cells were subjected to hypoxic reoxygenation (HR) to simulate the microenvironment of IRI. Intracellular NO release was assessed by using 4-aminomethyl-2', 7'-dichlorofluorescein diacetate (DAF-FM DA, NO probe). As shown in Figure S11, NO SOD/PA@

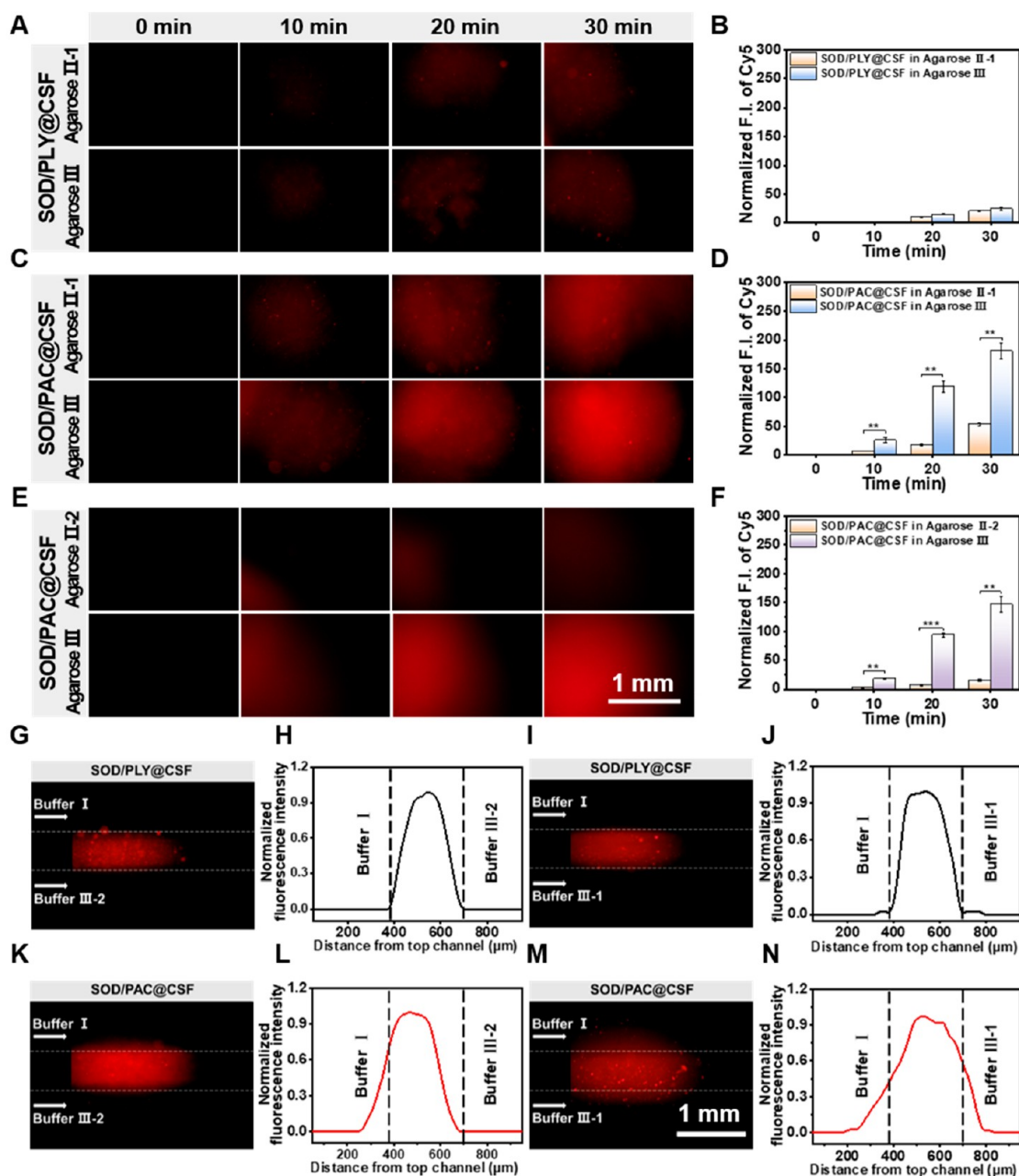


Figure 3. Evaluation of the chemotaxis behavior of SOD/PAC@CSF nanomotors in static and dynamic environments. The fluorescence images and corresponding quantified fluorescence intensity of (A and B) SOD/PLY@CSF, (C and D) SOD/PAC@CSF in reservoir (II-1) and (III), and (E and F) SOD/PAC@CSF in reservoir (II-2) and (III) of the Y-shaped channel. Representative fluorescence images and corresponding normalized fluorescence intensity of SOD/PLY@CSF flow in the presence of (G and H) buffer I and buffer III-2, and (I and J) buffer I and buffer III-1 on two sides. Representative fluorescence images and corresponding normalized fluorescence intensity of SOD/PAC@CSF flow in the presence of (K and L) buffer I and buffer III-2, and (M and N) buffer I and buffer III-1 on both sides. Experimental data are means \pm SD of samples in a representative experiment ($n = 3$). * $P < 0.05$, ** $P < 0.01$, and *** $P < 0.001$, determined by Student's t test.

CSF and NO/H₂S SOD/PAC@CSF nanomotors containing M-Arg (which can generate NO) showed relatively strong fluorescence signals (high NO concentration). In comparison to the untreated H9c2 cell, the detected NO remained essentially stable in the model and non-nanomotor SOD/PLY@CSF nanoparticle group (Figure S12). When the NO SOD/PA@CSF and SOD/PC@CSF nanomotors were perturbed, the cellular NO was increased by 6.0-fold and 2.9-fold, respectively. In the NO/H₂S SOD/PAC@CSF

nanomotor group, NO was increased to about 5.5-fold. Since the non-nanomotor SOD/PLY@CSF NPs cannot generate H₂S, the intracellular H₂S content of SOD/PLY@CSF treated H9c2 cells is comparable to that of untreated H9c2 cells (289.0 nM). In contrast, the intracellular H₂S content in H9c2 cells treated with SOD/PC@CSF nanomotors containing M-Cys and SOD/PAC@CSF nanomotors (which can generate H₂S) increased significantly to 671.2 and 660.2 nM, respectively (Figure S13). It can be found that the NO/H₂S nanomotors

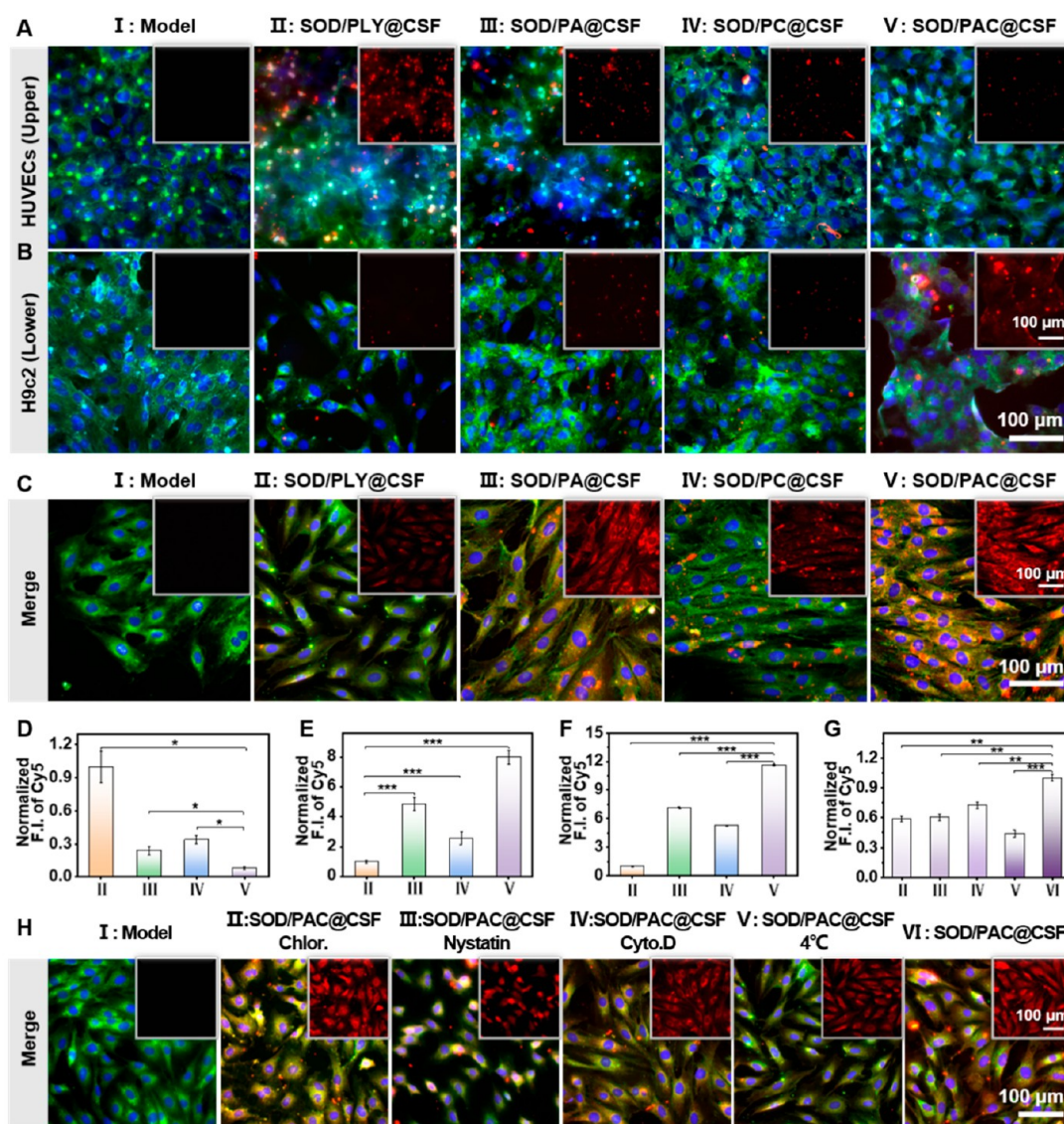


Figure 4. Cellular uptake performance of SOD/PAC@CSF nanomotors. Fluorescence images of (A) HUVECs (upper layer of Transwell) and (B) HR-injured H9c2 cells (lower layer of Transwell). (C) Fluorescence images of cellular uptake of different samples in HR-injured H9c2 cells (I: Model, II: SOD/PLY@CSF, III: SOD/PA@CSF, IV: SOD/PC@CSF, V: SOD/PAC@CSF). (D, E, and F) The normalized fluorescence quantitative results for A, B, and C. (G and H) The normalized fluorescence quantitative results and fluorescence images of cellular uptake of SOD/PAC@CSF in HR-injured H9c2 cells after 4 h treatment in the absence or presence of different endocytic inhibitors (Chlor. (chlorpromazine), nystatin, Cyto. D (cytochalasin D) and 4 °C; I: Model, II: SOD/PAC@CSF with Chlor., III: SOD/PAC@CSF with Nystatin, IV: SOD/PAC@CSF with Cyto. D, V: SOD/PAC@CSF coincubated with cells at 4 °C, VI: SOD/PAC@CSF). (Blue, nucleus stained with Hoechst 33342; red, cy5-labeled samples; green, cell membrane stained with DiO; the inserted images represent the single channel of different samples). Experimental data are means \pm SD of samples in a representative experiment ($n = 3$). * $P < 0.05$, ** $P < 0.01$, and *** $P < 0.001$, determined by one-way ANOVA.

had a more significant motion capability compared to those of the NO nanomotors and H₂S nanomotors, even though the gas production of NO and H₂S was not significantly increased.

Chemotactic Performance of the Nanomotors. The chemotactic behavior of the NO/H₂S SOD/PAC@CSF nanomotors to a high level of ROS and iNOS is the prerequisite basis of its targeting to the IRI site. Here, the chemotactic behavior of the NO/H₂S SOD/PAC@CSF nanomotors was evaluated using a static Y-shaped microfluidic channel model and a dynamic microfluidic model. Using cy5-labeled SOD/PLY@CSF (containing a reference substance M-Lys which does not participate in endogenous reaction, non-nanomotor) as control, we tested the chemotactic behavior of

cy5-labeled SOD/PAC@CSF nanomotors (containing endogenous reaction substrate M-Arg, NO/H₂S nanomotors) to a high concentration of ROS and iNOS in the cellular environment.

As shown in the schematic diagram of the static Y-shaped microfluidic channel model (Figure S14), chambers I, II, and III respectively include fluorescently labeled sample I, agarose gel II-1 blended normal H9c2 cell lysate (without high-expressed ROS and iNOS) or agarose gel II-2 blended PBS only, and agarose gel III blended prestimulated H9c2 cell lysate (containing chemical attractants, high-expressed ROS and iNOS, which can induce chemotaxis of nanomotors). After cy5-labeled SOD/PLY@CSF or cy5-labeled SOD/PAC@CSF

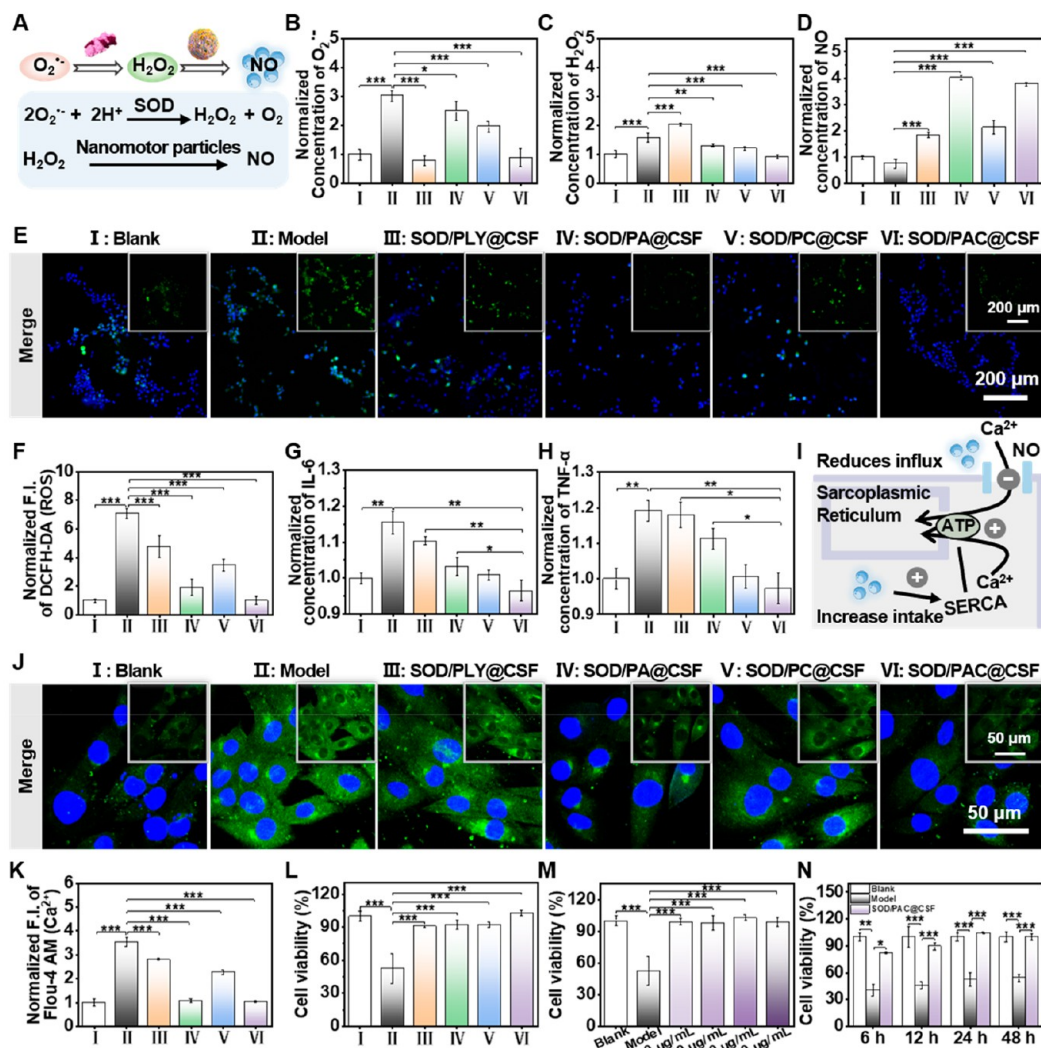


Figure 5. NO/H₂S SOD/PAC@CSF nanomotors alleviate oxidative stress and protect cardiomyocytes through the cascade effect *in vitro*. (A) Schematic illustration of SOD/PAC@CSF mediating the elimination of ROS and production of NO through the cascade effect. The normalized concentration of (B) O₂^{•-} and (C) H₂O₂ in the H9c2 cell environment after different sample treatments. (I: Blank; II: Model; III: SOD; IV: M-Arg; V: PAC@CSF; VI: SOD/PAC@CSF). (D) The normalized concentration of NO in the H9c2 cell environment after different sample treatments. (E) Fluorescence images and (F) the normalized fluorescence quantitative results of ROS changes in H9c2 cells after different sample treatments (blue, nucleus stained with Hoechst 33342; green, ROS stained with DCFH-DA). (G) IL-6 and (H) TNF- α levels in the H9c2 cell after different sample treatments. (I) Diagram of SOD/PAC@CSF relieving Ca²⁺ overload. (J) Fluorescence image and (K) normalized fluorescence quantitative results of Ca²⁺ changes in H9c2 cells after different sample treatments (blue, nucleus stained with Hoechst 33342; green, Ca²⁺ stained with Flou-4 AM; the inset image shows the separate channel for different samples). (I: Blank; II: Model; III: SOD/PLY@CSF; IV: SOD/PA@CSF; V: SOD/PC@CSF; VI: SOD/PAC@CSF). (L) Cell viability of HR-injured H9c2 cells treated with different samples. (M) Cell viability of HR-injured H9c2 cells treated with SOD/PAC@CSF nanomotors at different concentrations for 24 h. (N) Cell viability of HR-injured H9c2 cells treated with SOD/PAC@CSF nanomotors for different times (200 $\mu\text{g mL}^{-1}$). Experimental data are means \pm SD of samples in a representative experiment ($n = 3$). * $P < 0.05$, ** $P < 0.01$, and *** $P < 0.001$, determined by one-way ANOVA.

was added to chamber I, the fluorescence images of chambers II-1 and III were acquired by CLSM at 10, 20, and 30 min, and the corresponding normalized fluorescence intensities were calculated (Figure 3A–D). When chamber I was added with the non-nanomotor SOD/PLY@CSF NPs, and chambers II and III were added with agarose gel blended with normal H9c2 cell lysate and agarose gel blended with prestimulated H9c2 cell lysate, respectively, the normalized fluorescence intensity of chamber II and chamber III is not significantly different (both less than 30) due to the lack of motion, whereas when chamber I was added with the NO/H₂S SOD/PAC@CSF nanomotors, and chambers II and III were added with agarose

gel blended with normal H9c2 cell lysate and with prestimulated H9c2 cell lysate, respectively, the fluorescence intensity of chamber III gradually increased. After 30 min, the fluorescence intensity of chamber II and chamber III was significantly different (the latter was about three times that of the former), which can be attributed to the chemotactic behavior of the NO/H₂S nanomotors SOD/PAC@CSF in response to the high expression of ROS and iNOS in chamber III. Similarly, when chamber I was still added with the NO/H₂S SOD/PAC@CSF nanomotors, and chambers II and III were PBS and agarose gel blended with prestimulated H9c2 cell lysate, respectively, there is a significant difference in

fluorescence between chamber II and chamber III after 30 min, which is also likely to be attributed to the chemotaxis of the nanomotors (Figure 3E, F).

Furthermore, we established a dynamic microfluidic model as shown in Figure S15 to investigate the chemotaxis ability of nanomotors in a flowing state. Buffers I, II, and III contain prestimulated H9c2 cell lysate (containing chemical attractants, high-expressed ROS and iNOS), cy5-labeled samples, and normal H9c2 cell lysate (buffer III-1, without high-expressed ROS and iNOS) or only PBS (buffer III-2), respectively. CLSM is used to observe the state of Buffer II (middle section), which contains the fluorescently labeled sample dispersed at a distance of 22 mm from the inlet. When cy5-labeled SOD/PLY@CSF is added to buffer II, regardless of whether the fluids on both sides are buffer I and buffer III-2 or buffer I and buffer III-1, the red fluorescence does not obviously shift, because SOD/PLY@CSF has no ability to move (Figure 3G–J). When cy5-labeled SOD/PAC@CSF is added to buffer II and the fluids on both sides are buffer I and buffer III-2, that is, one side contains a chemical attractant and the other side is PBS (Figure 3K), the red fluorescence center of cy5-labeled SOD/PAC@CSF has a movement compared with the red fluorescence center of cy5-labeled SOD/PLY@CSF changes, and it shifts to buffer I by about 73.0 μm (Figure 3L). Similarly, when the fluids on both sides are buffer I and buffer III-1, one side containing chemical attractants and the other side without chemical attractants (Figure 3M), the red fluorescence center representing SOD/PAC@CSF also shifts to buffer I more obviously (Figure 3N). The above results demonstrated that the NO/H₂S nanomotors SOD/PAC@CSF can still show obvious chemotaxis to microenvironments with high expression of ROS and iNOS under fluid conditions.

Cellular Uptake of the Nanomotors. The motion behavior of the nanomotors is very favorable for its efficient uptake by cells,^{51–53} and we next evaluated these properties. First, the capability of the NO/H₂S SOD/PAC@CSF nanomotors to penetrate human venous endothelial cells (HUVECs) was assessed. We used a two-dimensional Transwell experimental model to simulate the barrier between blood and heart tissue, where the upper layer was grown with HUVECs and the lower layer was grown with H9c2 cells, both of which have undergone HR injury (Figure S16). Cells were treated with cy5-labeled different samples, and the red fluorescence intensity of the upper and lower chambers of each group was observed by CLSM (Figure 4A and B, S17 and S18). Compared to non-nanomotor SOD/PLY@CSF NPs, NO SOD/PA@CSF nanomotors and H₂S SOD/PC@CSF nanomotors showed a slightly improved penetration ability. The NO/H₂S SOD/PAC@CSF nanomotors showed the best penetration ability, with intensity decreasing to a minimum in the upper chamber and increasing to a maximum in the lower chamber. Fluorescence images of the cellular uptake assay also showed a more prominent red fluorescence signal in cells cultured with the NO/H₂S SOD/PAC@CSF nanomotors (Figure 4C, S19). The normalized fluorescence quantification results for the above assays show similar trends. In the Transwell assay, treatment with NO/H₂S SOD/PAC@CSF nanomotors decreased the red fluorescence of cells in the upper chamber to 0.1-fold and increased the fluorescence in the lower chamber to 11.6-fold compared to non-nanomotor SOD/PLY@CSF NPs (Figure 4D and E). In terms of cellular uptake, compared to the non-nanomotor SOD/PLY@CSF NPs, the fluorescence intensity of the nanomotors reached 4.8-

fold (NO SOD/PA@CSF nanomotors) and 2.6-fold (H₂S SOD/PC@CSF nanomotors), respectively, while the fluorescence intensity of the NO/H₂S SOD/PAC@CSF nanomotor group reached 8.0-fold (Figure 4F). Both the normalized quantitative results and the fluorescence images showed significant differences in the cellular uptake efficiency of HR-injured H9c2 cells after treatment with uptake pathway inhibitors Chlor. (chlorpromazine, an inhibitor of the clathrin-mediated pathway), Nystatin (an inhibitor of the caveolin-mediated pathway), Cyto. D (cytochalasin D, an inhibitor of the macropinocytosis pathway), and 4 °C (an energy inhibitor), respectively.^{54–57} The ability of H9c2 cells to take up SOD/PAC@CSF nanomotors was partially inhibited by Chlor., nystatin, and Cyto. D to approximately 0.7-fold compared to the nanomotors group without endocytosis inhibitor (Figure 4G). This indicates that the pathway of the nanomotors into cells is likely to be more complex, involving multiple pathways, with clathrin-mediated, caveolin-mediated, and macropinocytosis pathways all being involved. Cellular uptake of the nanomotors was also minimal at 4 °C, reduced to ~0.4-fold (Figure 4G), and the red fluorescence intensity of the cells treated at 4 °C was relatively weak (Figure 4H, S20), which may be due to reduced metabolic rates and cell membrane fluidity at low temperatures, resulting in a blocked energy-dependent endocytosis.⁵⁷

In Vitro Protection Effect of the Nanomotors on Cardiomyocytes. After confirming that the motion effect of nanomotors is effective in promoting their absorption by cells, we then tested whether the nanomotors could effectively play a therapeutic role in HR-injured cells. In this system, the covalently bonded SOD and M-Arg in the NO/H₂S SOD/PAC@CSF nanomotors can eliminate the ROS component through a cascading effect, as shown in Figure 5A, where the SOD can catalyze the production of O₂^{•-} to H₂O₂, which can then be used as a reaction substrate to react with M-Arg and be further consumed to produce NO. As shown in Figure 5B and C, O₂^{•-} and H₂O₂ in the cells were increased to 3.0-fold and 1.6-fold, respectively, after HR injury compared to the blank group. After SOD treatment, O₂^{•-} could be approximately restored to that of the O₂^{•-} fraction of normal cells, but a large amount of H₂O₂ was produced (increased to 2.0-fold). The PAC@CSF group containing only M-Arg (no cascading effect) consumed an amount of O₂^{•-} and H₂O₂ that was reduced to 1.9-fold and 1.2-fold, respectively. The SOD/PAC@CSF nanomotors with cascading effect consumed a significant amount of O₂^{•-} while reducing H₂O₂ levels to levels comparable to normal cells. Correspondingly, the level of NO in cells after HR injury was reduced to 0.8-fold compared to that of the blank group, while the SOD/PA@CSF and SOD/PAC@CSF nanomotors were able to contribute to a 4.0 and 3.8-fold increase in NO, respectively (Figure 5D). Total cellular ROS content was also characterized by staining with 2',7'-dichlorofluorescein diacetate (DCFH-DA, ROS probe) to assess the contribution of the cascading effect to ROS reduction by the nanomotors. As shown in Figure 5E and S21, ROS fluorescence intensity was significantly enhanced in cells after HR injury, and the SOD/PA@CSF and SOD/PC@CSF groups without a cascading effect could reduce the intracellular ROS content to some extent, while the NO/H₂S SOD/PAC@CSF nanomotors with a cascading effect showed the best ROS scavenging ability with significantly reduced fluorescence intensity. The quantitative results shown in Figure 5F show a similar trend, with the NO/H₂S SOD/PAC@CSF

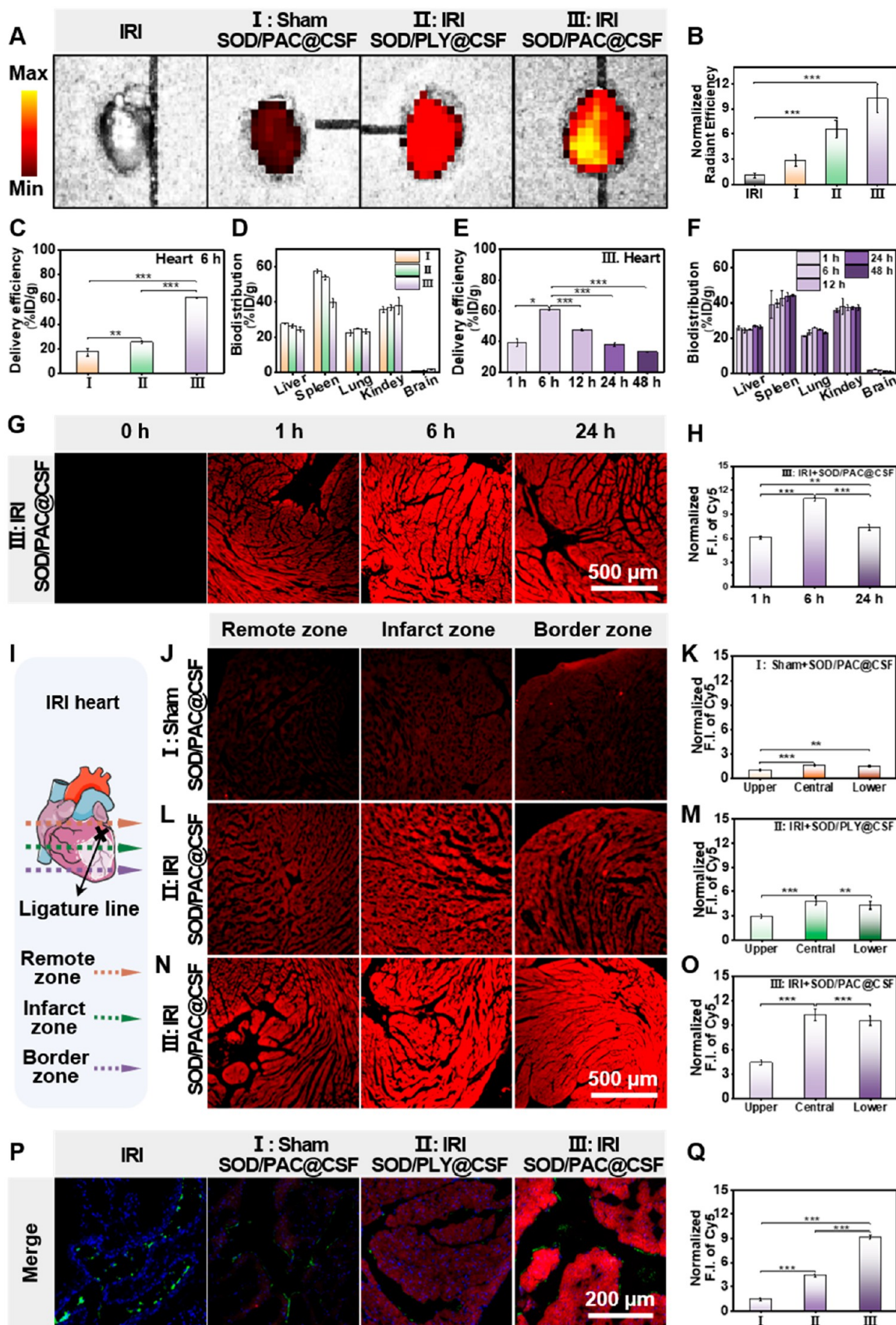


Figure 6. *In vivo* heart accumulation and biodistribution of cy5-labeled SOD/PAC@CSF in IRI model mice that were injected with cy5-labeled SOD/PAC@CSF or cy5-labeled SOD/PLY@CSF via tail vein, heart, and major organs, which were harvested for *ex vivo* imaging at different time points. (A) Representative *ex vivo* fluorescence images and (B) quantification results for cy5-labeled NPs in the heart of mice

Figure 6. continued

after 6 h of injection of different samples. Biodistribution of different samples in (C) heart and (D) other organs. Biodistribution of cy5-labeled SOD/PAC@CSF in (E) heart and (F) other organs after intravenous injection for different times. (G) Fluorescence images and (H) corresponding normalized fluorescence intensity of cy5 labeled SOD/PAC@CSF at different times after administration. (I) Schematic diagram of the ligature position of the mouse heart IRI model. After injection of material, the heart was divided into remote zone, infarct zone, and border zone for frozen sectioning. Fluorescence images and corresponding normalized fluorescence of remote zone, infarct zone, and border zone of the heart accumulation effect of (J and K) I, (L and M) II, and (N and O) III group after 6 h of injection. (P) Immunofluorescence images and (Q) corresponding normalized fluorescence results of the distribution of cy5-labeled samples in the infarct zone of the heart in I, II, and III group after 6 h of injection. (Green, vessel stained with CD31; blue, nucleus stained with DAPI; red, cy5-labeled samples). Experimental data are means \pm SD of samples in a representative experiment ($n = 3$). * $P < 0.05$, ** $P < 0.01$, and *** $P < 0.001$, determined by one-way ANOVA.

nanomotors reducing the ROS level to the lowest level, about one-seventh of the model group (comparable to the normal intracellular ROS level).

After confirming that SOD/PAC@CSF nanomotors efficiently enter H9c2 cells and responsively eliminate ROS, alleviate oxidative stress, and release NO (Figure 5E, S11 and S12) and H₂S (Figure S13), while maintaining high activity of G-CSF (Figure 2G) and SOD (Figure 2H), we further investigated their efficacy in reducing inflammation, alleviating calcium overload, and improving cell viability.

First, the consumption of ROS and release of H₂S during nanomotor movement may have an effect on the resolution of inflammation. For example, H₂S may inhibit the NF- κ B (nuclear factor kappa-B) pathway, reduce inflammatory cell infiltration caused by pro-inflammatory factors, and induce neutrophil apoptosis and macrophage switch to an anti-inflammatory phenotype, thereby exerting myocardial protective effects.^{58,59} As shown in Figure 5G and H, cells treated with the NO/H₂S SOD/PAC@CSF nanomotors showed a significant reduction in intracellular inflammatory factors (IL-6 and TNF- α were selected as important factors in the inflammatory storm),^{60,61} which basically returned to normal cell levels.

In addition, during the reduction of oxidative stress by the nanomotors, NO is released, which reduces Ca²⁺ influx by inhibiting the opening of L-type Ca²⁺ channels and promoting the opening K_{ATP} channels. On the other hand, it acts on soluble guanylate cyclase (sGC), stimulating cGMP signaling and increasing Ca²⁺ uptake by increasing SERCA activity, that together reduce HR-induced calcium overload (Figure 5I). H9c2 cells were stained with Fluo-4 AM (Ca²⁺ probe) after nanomotor treatment, as shown in Figure 5J, S22, and the fluorescence intensity representing Ca²⁺ content was significantly decreased. By normalized fluorescence quantitative results (Figure 5K), the Ca²⁺ content of the model group increased up to 3.5-fold compared to that of the blank group. The non-nanomotor SOD/PLY@CSF NPs group, which partially alleviated cellular oxidative stress due to the presence of SOD, showed a slight reduction in Ca²⁺ levels compared to the model group, while both the non-nanomotor SOD/PA@CSF and SOD/PC@CSF nanomotor groups showed a reduction in Ca²⁺ levels. The NO/H₂S SOD/PAC@CSF nanomotors reduced Ca²⁺ levels to the level of the blank group by releasing NO. The NO/H₂S SOD/PAC@CSF nanomotors maximally relieved the calcium overload and prompted a return of intracellular Ca²⁺ levels to essentially normal levels.

The above functions of the nanomotors help to promote the repair of HR-injured H9c2 cells, so we next assessed cell viability. As shown in Figure S23A, the components involved in the preparation of the SOD/PAC@CSF nanomotors

showed no significant toxicity to normal H9c2 cells, and the cells all maintained high cell viability (above 90.0%). For the SOD/PAC@CSF nanomotors, we also evaluated the cytotoxicity of different doses (50–400 $\mu\text{g mL}^{-1}$) and different incubation times (6–48 h) on normal H9c2 cells. Cell viability decreased slightly with increasing concentration but remained above 90.0%, and cells maintained high activity with increasing time (Figure S23B and C). The cellular activity of H9c2 cells after HR injury decreased significantly ($\sim 50.0\%$), whereas for SOD/PLY@CSF, SOD/PA@CSF, SOD/PC@CSF, and SOD/PAC@CSF nanomaterials and different concentrations (50–400 $\mu\text{g mL}^{-1}$) of SOD/PAC@CSF nanomotors co-incubated with HR-injured H9c2 cells for 24 h, the cells all maintained high activity (above 90.0%) (Figure 5L and M). With increasing coincubation time (6–48 h), SOD/PAC@CSF nanomotors gradually increased the viability of HR-injured H9c2 cells and largely returned to normal levels (Figure 5N). These results all support that the NO/H₂S SOD/PAC@CSF nanomotors, by depleting ROS, reducing inflammatory factor levels, and alleviating calcium overload, have a significant promoting effect on the repair of HR injured H9c2 cells. We also evaluated the pro- and antiapoptotic proteins of the cells during this process. It is well-known that the onset of apoptosis is antagonistically regulated by intracellular anti-apoptotic proteins (Bax) and proapoptotic proteins (Bcl2).^{62,63} While cleaved caspase-3 (CC3) is the key downstream apoptotic protease regulated by the Bax/Bcl2 ratio, activation of CC3 leads to apoptosis.⁶⁴ Western blot analysis showed that G-CSF, SOD/PAC and SOD/PAC@CSF nanomotors all significantly downregulated the expression of Bax, upregulated the expression of Bcl2 and ultimately decreased the Bax/Bcl2 ratio and CC3, as the regulatory feedback from the microenvironment of HR-injured cells is complex (Figure S24). Overall, the significant reduction in apoptotic cardiomyocytes contributed to better recovery of cardiac function in IRI.

In Vivo Targeting Capability of the Nanomotors. The above results have demonstrated that the nanomotors constructed in this work are capable of significant positive chemotaxis to high concentrations of ROS produced by IRI cardiomyocytes and are effectively taken up by cardiomyocytes. In this section, we use a mouse IRI model to verify whether this chemotactic ability can help the nanomotors achieve effective targeting and high retention at the site of the IRI *in vivo*. First, to visually demonstrate the targeting effect of nanomotors on the mouse heart, *in vitro* imaging was used to detect the accumulation of nanomotors (Figure 6A, S25). There was some accumulation of SOD/PLY@CSF, which has no chemotactic targeting function, at the heart site after 6 h of injection of various cy5-labeled NPs into the mice. This may

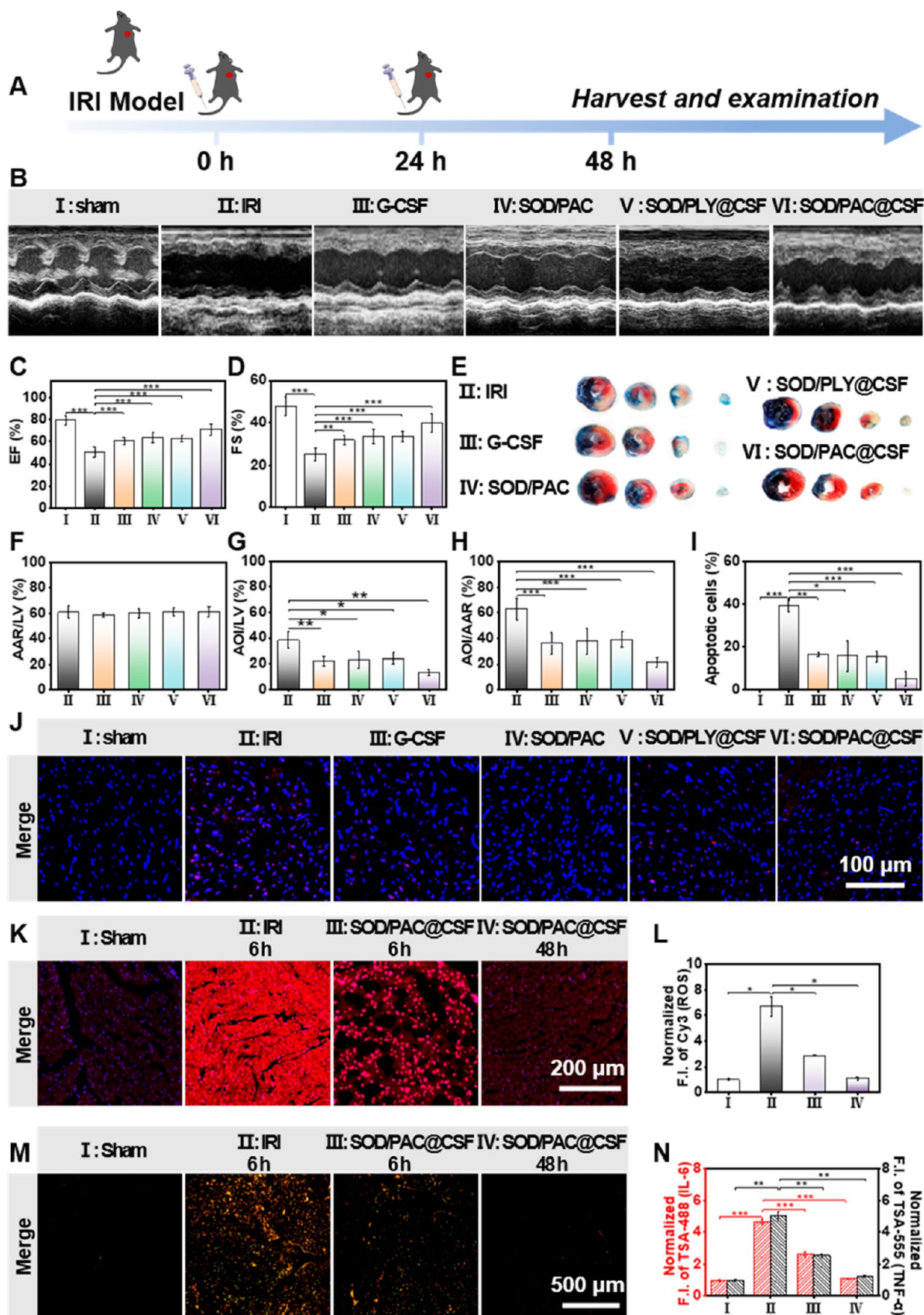


Figure 7. *In vivo* therapeutic effect of SOD/PAC@CSF nanomotors in IRI heart of mice. (A) Schematic illustration of the IRI model and tail vein injection of the therapeutic agent at 0 and 24 h in mice. (B) Representative echocardiographic images, (C) ejection fractions (EF), and (D) fractional shortening (FS) after injection of different samples. (E) Representative images of triphenyltetrazolium chloride (TTC) double staining from the basal, midleft ventricular (LV), and apical regions of the hearts 2 days after injection of different samples. The percentage

Figure 7. continued

of (F) area at risk (AAR) and (G) area of infarction (AOI) in the left ventricle (LV). (H) The percentage of AOI over AAR to represent the area of infarction. (I) Quantitative analysis and TUNEL positive cells and (J) immunofluorescence images of TUNEL staining injected with different samples (red, apoptotic cells stained with TUNEL; blue, normal cells stained with DAPI) (I: Sham, II: IRI, III: G-CSF, IV: SOD/PAC, V: SOD/PLY@CSF, VI: SOD/PAC@CSF) ($n = 6$). Immunofluorescence images and corresponding normalized fluorescence of (K and L) ROS and (M and N) IL-6 and TNF- α changes in the IRI heart at 6 and 48 h after injection of SOD/PAC@CSF. (I: Sham, II: IRI, III: 6 h after injection of SOD/PAC@CSF, IV: 48 h after injection of SOD/PAC@CSF; blue, nucleus stained with DAPI; red, ROS stained with cy3; green, IL-6 stained with TSA-488; orange, TNF- α stained with TSA-555) ($n = 3$). Experimental data are means \pm SD of samples in a representative experiment. * $P < 0.05$, ** $P < 0.01$, and *** $P < 0.001$, determined by one-way ANOVA.

be due to the fact that the heart provides the pressure for blood flow to different parts of the body, so drugs injected intravenously accumulate in the heart and are subsequently delivered to other sites.^{35,65} In contrast, SOD/PAC@CSF nanomotors with chemotactic targeting ability showed a very strong fluorescence signal, which was not present in the sham group (mice were not modeled with IRI but injected with cy5-labeled SOD/PAC@CSF nanomotors), suggesting that the effective accumulation of SOD/PAC@CSF nanomotors in the hearts of IRI mice is closely related to the high expression of ROS and iNOS at this site. Further fluorescence quantification results also confirmed the above conclusion that the fluorescence intensity of SOD/PAC@CSF nanomotors in the hearts of IRI model mice was 10.2-fold that of the sham group (Figure 6B).

Second, to more comprehensively evaluate the targeting performance of nanomotors in whole organs, we analyzed the accumulation and *in vivo* biodistribution of different materials in IRI mouse hearts by grinding the whole organ and measuring its total fluorescence intensity. As shown in Figure 6C, compared with groups I and II (cardiac accumulation of 17.4% ID/g and 25.2% ID/g, respectively), the accumulation of SOD/PAC@CSF nanomotors in the IRI heart of mice in group III increased to 61.2% ID/g after 6 h. Meanwhile, SOD/PAC@CSF nanomotors showed a lower proportion of distribution in other organs compared to SOD/PLY@CSF NPs that did not have a chemotactic targeting function (Figure 6D). Furthermore, the biodistribution of SOD/PAC@CSF nanomotors in the heart and major organs of IRI model mice over time was also examined, as shown in Figure 6E, where a fluorescent signal could be measured in the heart at 1 h after injection, with a further increase in signal intensity in the heart at 6 h, followed by a gradual decrease in fluorescence intensity and a similar trend of fluorescence accumulation in the other major organs (Figure 6F). This clearly indicates that the nanomotors enhance the rapid and precise targeting of the drug to the IRI heart and enable long-lasting accumulation, which is essential for recovery of the injured tissue. In particular, we also examined the fluorescence intensity of sections of the infarct zone of the mouse heart after injection of cy5-labeled SOD/PAC@CSF nanomotors at different times and found that the fluorescence signal could be measured in the infarct zone at 1 h. The fluorescence signal intensity further increased at 6 h and remained at 24 h. The quantitative results showed the same trend (Figure 6G and H).

As mentioned above, intravenously administered drugs preferentially accumulate in the heart and are subsequently transported throughout the body; therefore, accumulation in the heart does not necessarily mean effective targeting of the IRI site. In this section, we looked at sections for different parts of the heart to assess the accumulation of different materials in different locations.

We divided the heart into three parts according to the remote zone, infarct zone, and border zone, with the infarct zone representing the ligated area (Figure 6I). From the fluorescence images and normalized results, the fluorescence accumulation in all parts of the heart of mice in groups I and II was weak, and the difference in fluorescence intensity of the material in different parts of the heart was not significant (Figure 6J–M), whereas group III showed the precise targeted accumulation of SOD/PAC@CSF nanomotors in the IRI region, with comparable fluorescence intensity in the infarct and border zone (IRI region), which was about twice as high as in the remote zone (healthy region) (Figure 6N and O). The fluorescence intensities of the remote, infarct, and border zones were also normalized separately for groups I, II, and III. Fluorescence accumulation was generally stronger in group III than in groups I and II, with the difference between group III and groups I and II being particularly significant in the infarct and border regions (IRI regions), reaching approximately 9.5 and 4.3-fold, respectively (Figure S26, S27, and S28).

Finally, we examined the tissue penetration of the nanomotors in areas of the IRI in the mouse heart. The distribution of nanomaterials around vessels and overall in each group was observed by immunofluorescence staining to label vessels (green, vessel marker CD31 and stained with Alexa Fluor 488). As shown in Figure 6P, S29, the total and perivascular fluorescence intensity was generally darker in groups I (without high ROS and iNOS microenvironment) and II (non-nanomotor SOD/PLY@CSF nanomaterials, no chemotactic effect), whereas in group III (high ROS microenvironment, SOD/PAC@CSF nanomotors with chemotactic effect) the center of the IRI heart was almost filled with red fluorescence, with significantly increased infiltration capacity. The total fluorescence intensity was increased to 9.2-fold (Figure 6Q). This result suggests that the SOD/PAC@CSF nanomotors has a good vascular penetration ability due to the chemotaxis of the high ROS microenvironment with the help of autonomous movement and eventually targets and accumulates in the tissues of the IRI heart region.

In Vivo Therapeutic Effects of the Nanomotors. The pharmacokinetics of the SOD/PAC@CSF nanomotors was investigated before assessing their therapeutic efficacy *in vivo*. As shown in Figure S30, the binding of G-CSF to the nanomotors resulted in a significantly longer half-life (~ 3 h) compared to that of free G-CSF (less than ~ 0.5 h), which facilitated a better antiapoptotic function of G-CSF. Subsequently, to test the therapeutic efficacy of the SOD/PAC@CSF nanomotors, IRI mice were injected via the tail vein with pure drug G-CSF, drug-free SOD/PAC nanomotors, non-nanomotor but drug-loaded SOD/PLY@CSF NPs, or chemotactic and drug-loaded SOD/PAC@CSF nanomotors at the time of IRI and 24 h later (Figure 7A). Echocardiography was performed 2 days postoperatively, and the images showed

varying degrees of change in systolic function in the anterior/posterior left ventricular wall of IRI mice after treatment with different materials (Figure 7B). Quantitative analysis showed a significant decrease in cardiac function in the IRI group (Ejection fractions (EF): 50.4%; Fractional shortening (FS): 25.0%) compared to the sham group (EF: 79.5%; FS: 47.7%). G-CSF is able to resist cardiomyocyte apoptosis, while SOD/PAC and SOD/PLY@CSF have some ability to alleviate oxidative stress. Thus, G-CSF (EF: 60.5%; FS: 31.9%), SOD/PAC (EF: 63.5%; FS: 33.5%), and SOD/PLY@CSF (EF: 62.9%; FS: 33.4%) contributed to a gradual improvement in cardiac function. In contrast, SOD/PAC@CSF nanomotors (EF: 71.0%; FS: 39.8%) showed the most significant improvement in cardiac function, with recovery of cardiac function to a level comparable to that of the sham group (Figure 7C and D). It is not difficult to speculate that the more precise targeting and longer retention of the SOD/PAC@CSF nanomotors at the site of IRI facilitate its therapeutic effect. Next, we used triphenyltetrazolium chloride (TTC) staining to observe the area of the heart injury region in mice (Figure 7E). The blue area is the normal area, and the rest of the area (both white and red) is the area at risk (AAR), where the white area is the area of infarction (AOI) and the red area is the ischemic but noninfarcted area. It can be seen that the IRI group has the largest proportion of red and white areas in the heart with a smaller proportion of blue areas. The AAR was relatively reduced after G-CSF, SOD/PAC and SOD/PLY@CSF treatment, and the vast majority of the AAR improved after SOD/PAC@CSF nanomotor treatment, as the heart basically returned to normal. In turn, AAR as a percentage of left ventricle (LV) (AAR/LV), AOI as a percentage of LV (AOI/LV) and AOI as a percentage of AAR (AOI/AAR) were calculated (Figure 7F–H). Compared with the IRI group (AAR/LV: 60.8%; AOI/LV: 38.2%; AOI/AAR: 62.7%), myocardial infarction was significantly improved in SOD/PAC@CSF nanomotor-treated mice (AAR/LV: 61.0%; AOI/LV: 13.0%; AOI/AAR: 21.4%), indicating that SOD/PAC@CSF nanomotors have good therapeutic effects.

To further investigate the antiapoptotic effect of SOD/PAC@CSF nanomotors, we sectioned the LV 48 h after IRI and stained it by Terminaldeoxynucleotidyltransferase-mediated dUTP-Xnickend-labeling (TUNEL) to label apoptotic cells (Figure 7I, 7J, and S31). Compared to the sham group, the number of TUNEL-positive nuclei (red) increased significantly in IRI mice, and the percentage of apoptotic cells rose from 0.2% to 39.4%. After treatment with G-CSF, SOD/PAC, and SOD/PLY@CSF nanomaterials, the percentage of apoptotic cells was reduced to 16.5%, 15.8%, and 15.4%, respectively. And the antiapoptotic effect of the SOD/PAC@CSF nanomotors group was significantly increased and the proportion of apoptotic cells (5.4%) was significantly reduced, close to that of the sham group. The expression of CC3 protein, which plays an important role in apoptosis, was next examined by Western blot analysis (Figure S32). CC3 expression was significantly higher in the IRI group than in the Sham group, whereas G-CSF, SOD/PAC and SOD/PLY@CSF nanomaterial treatments all reduced it, and the SOD/PAC@CSF nanomotors group induced a reduction to the level of the Sham group. This suggests that SOD/PAC@CSF nanomotors more comprehensively reverse the apoptotic tendency of injured cardiomyocytes.

Finally, we assessed the ability of SOD/PAC@CSF nanomotors to scavenge ROS and reduce inflammatory levels

in mouse IRI mice tissue after 6 and 48 h of SOD/PAC@CSF nanomotors injection. Immunofluorescence staining for ROS was performed on the IRI heart sections (Figure 7K, S33), and it can be observed that the strongest red fluorescence signal representing ROS was observed in the IRI group, and the fluorescence signal was significantly reduced after 6 h of SOD/PAC@CSF nanomotors treatment, which may be owing to the fact that at this time the nanomotors achieved strong targeting of the IRI heart and was able to cascade the elimination of ROS; after 48 h, the fluorescence signal decreased to no different from the sham group, marking the return of ROS levels in the IRI heart to normal levels, with quantitative results showing a similar trend (Figure 7L). Furthermore, the development of inflammation largely mediates the progression of IRI tissue, for example, upregulation of the inflammatory factors IL-6 and TNF- α positively correlates with the area of myocardial necrosis.^{66,67} IL-6 and TNF- α were observed and quantified by immunofluorescence labeling (Figure 7M, 7N, and S34). The IRI group showed a significant increase in the fluorescence signal representing IL-6 and TNF- α , which were 4.6 and 5.0-fold higher than those of the sham group, respectively. After 6 h of SOD/PAC@CSF nanomotor injection, the diminished fluorescence signal decreased to 2.6 and 2.5-fold of the sham group, and after 48 h, the fluorescence signal intensity and quantitative results decreased to the level of the sham group. A similar trend of reduction was observed in serum levels of IL-6 and TNF- α in IRI mice 6 and 48 h after SOD/PAC@CSF injection (Figure S35). The results presented above suggest that SOD/PAC@CSF can effectively reduce ROS and inflammation levels in IRI mouse tissues. This may be due to its cascading effect of alleviating oxidative stress and its release of NO, H₂S and G-CSF as therapeutic agents during exercise, which together participate in the repair process of injured myocardium.

DISCUSSION

The NO/H₂S SOD/PAC@CSF nanomotors we proposed offer irreplaceable advantages over both existing IRI therapeutics and existing G-CSF delivery systems, as described below.

In contrast to existing IRI therapeutics, the NO/H₂S SOD/PAC@CSF nanomotors prepared in this work intervene in the IRI process in a multifaceted and multilinked manner by reducing ROS, lowering inflammation levels, alleviating calcium overload, and directly resisting cardiomyocyte apoptosis. This is different from previous systems, and Table S1 summarizes the current methods used to treat IRI. For example, researchers alleviated oxidative stress by intracardiac injection of graphene oxide (GO)/alginate microgels,⁶⁸ ginsenoside Rg3 (Rg3) loaded with poly(ethylene glycol)-*b*-poly(propylene sulfide) (PEG-*b*-PPS) or the nanoenzyme Mito-Fenozyme with SOD- and CAT-like activity,^{69,70} reduced macrophage-mediated inflammation by intravenous injection of pioglitazone or TLR4 inhibitor (TAK-242) loaded with poly(lactic/glycolic acid) (PLGA) NPs,⁷¹ reduced the expression of inflammatory factors by intravenous injection of PLGA NPs-loaded immunosuppressant cyclosporine A (CsA),⁷² liposomal/neutrophil-loaded methotrexate (MTX),⁷³ and reduced intracellular Ca²⁺ influx in cardiomyocytes by coronary perfusion of PGMA NPs-loaded AID peptide.⁷⁴ Based on the complex feedback mechanism of IRI, theoretically, most of the above therapeutic systems target downstream lesion outcomes in the IRI process and it is

difficult to stop the continued production of upstream lesions, whereas we use NO/H₂S SOD/PAC@CSF nanomotors for precise targeted delivery of G-CSF, which can both directly upregulate the expression of antiapoptotic proteins in cardiomyocytes from upstream and also intervene downstream on pathological outcomes already generated, such as reducing ROS, lowering inflammatory levels, and alleviating calcium overload, allowing a more comprehensive treatment of IRI. In addition, we summarized the current H₂S and NO donor materials for the treatment of cardiovascular disease (Table S2). In comparison, we found that the current material design, which enables precise targeting to the site of IRI cardiac injury for drug delivery and simultaneous release of NO and H₂S via intravenous injection, has not been reported, and this NO/H₂S SOD/PAC@CSF nanomotor design provides a promising platform for intervention not only in IRI but also in other cardiovascular disease processes.

Compared to existing G-CSF delivery systems, the NO/H₂S SOD/PAC@CSF nanomotors not only provide a precise, targeted, and sustained delivery strategy for G-CSF to the site of cardiac injury, avoiding the side effects caused by systemic administration of G-CSF, but also play a microenvironmental regulatory role, facilitating G-CSF to better perform its repair function on cardiomyocytes. Unmitigated high ROS, high inflammation, and calcium overload in the IRI microenvironment led to microvascular occlusion, which largely limits the precise targeting of G-CSF to IRI sites and its antiapoptotic effect on cardiomyocytes. Therefore, in order for G-CSF to be fully effective, not only does it need to be effectively delivered to the injured areas of the heart, but also the adverse factors present in this microenvironment need to be eliminated as much as possible. Table S3 summarizes the methods currently used to deliver G-CSF. For example, researchers have improved the half-life of G-CSF in the blood and reduced the number of doses administered by functionalizing it with PEG, PLGA,^{31,75,76} or controlled the slow release of G-CSF using SiO₂, dextran or BSA NPs as carriers.^{33,77,78} On the one hand, none of the above delivery systems have attempted to deliver G-CSF to the heart site, and on the other hand, most of the carriers only play a single loading role and rarely involve microenvironmental modulation, making it difficult to use them directly for G-CSF delivery to the injured heart. With the SOD/PAC@CSF nanomotors, we delivered G-CSF precisely to the IRI site via a two-step targeting strategy. First, there was a specific affinity (enzyme–substrate interaction) between M-Arg in the SOD/PAC@CSF component and the highly expressed ROS/iNOS in the IRI microenvironment, which promoted effective chemotactic targeting and retention of SOD/PAC@CSF toward the IRI microenvironment. Subsequently, M-Arg and M-Cys in the SOD/PAC@CSF component underwent endogenous reactions to produce two gases, NO and H₂S, which promoted the autonomous movement of the SOD/PAC@CSF nanomotors, which enhanced G-CSF uptake by injured cardiomyocytes. At the IRI site, SOD and M-Arg in the SOD/PAC@CSF fraction can synergistically eliminate the high levels of ROS already present, H₂S generated by M-Cys can fundamentally reduce further expression of ROS and thus reduce the overall level of inflammation, and NO generated by M-Arg can alleviate calcium overload, so SOD/PAC@CSF can not only deliver G-CSF precisely but also modulate the IRI microenvironment so that G-CSF can better perform its function of repairing cardiomyocytes.

In addition, the SOD/PAC@CSF nanomotors, based on a dual-gas concept, are designed to prevent toxicity caused by high local concentrations of one particular gas while maintaining nanomotor propulsion. For example, low concentrations of NO (picomolar to nanomolar) are effective in promoting cell proliferation, maintaining vascular tone and blood pressure homeostasis, whereas high concentrations of NO (micromolar) disrupt key enzymes required for cellular metabolism and also react with superoxide to form more potent oxidants such as peroxynitrite, which mediates cytotoxicity.^{73,79–83} As shown in Figure 2N, the NO/H₂S nanomotors SOD/PAC@CSF increase the speed to approximately 180% without a significant increase in NO and H₂S gas production. Moreover, M-Arg in nanomotors can only consume the H₂O₂ already produced and cannot prevent the continued production of ROS. However, H₂S is able to inhibit ROS production and subsequent oxidative stress and inflammatory responses by stimulating GSH and thioredoxin activity and inhibiting the NF- κ B pathway.⁴¹ The synergistic effect between the NO/H₂S can better reduce the high expression of ROS in the disease microenvironment, which is also an advantage that single NO or H₂S nanomotors do not have.

CONCLUSIONS

The NO/H₂S SOD/PAC@CSF nanomotors for precise, targeted delivery and prolonged retention of G-CSF at the site of cardiac injury are constructed by a simple radical polymerization reaction. SOD converts surplus O₂^{•-} at the site of IRI into H₂O₂, which is subsequently consumed by M-Arg to produce NO. This cascade effect significantly reduces ROS levels; i.e., O₂^{•-} and H₂O₂ are restored to normal cellular levels. At the same time, the therapeutic gases NO and H₂S are released. With no significant increase in the amount of gas generated, the NO/H₂S nanomotors showed a significant increase in motility. Compared to non-nanomotor SOD/PLY@CSF NPs (less than 1.0 $\mu\text{m s}^{-1}$), NO SOD/PA@CSF nanomotors (3.1 $\mu\text{m s}^{-1}$), and H₂S SOD/PC@CSF nanomotors (2.9 $\mu\text{m s}^{-1}$), NO/H₂S SOD/PAC@CSF nanomotors (5.4 $\mu\text{m s}^{-1}$) show a more pronounced motility behavior in prestimulated H9c2 cells, making it more readily available for cellular uptake. Both the static Y-channel model (increased accumulation up to 9.8-fold in prestimulated H9c2 cell lysate compared to PBS) and the dynamic microfluidic model (73 μm offset toward prestimulated H9c2 cell lysate compared to PBS) confirmed the good chemotaxis of these nanomotors toward regions with high ROS/iNOS expression. The release of the therapeutic gas also reduced inflammation levels in HR-injured H9c2 cells, alleviated calcium overload, and reduced the Bax/Bcl2 ratio and CC3, ultimately increasing cell viability of HR-injured H9c2 cells (from about 50% to over 90%).

In this work, we also propose a delivery strategy that enables precise, targeted delivery and long-lasting retention of G-CSF at the site of cardiac injury. Compared to non-nanomotor SOD/PLY@CSF, *in vitro* cell transwell models (up to 11.6-fold increase in vascular endothelial cell transport efficiency) and *in vitro* cell uptake (up to 8.0-fold increase in uptake by HR-injured H9c2 cells) confirmed the importance of the NO/H₂S nanomotors SOD/PAC@CSF for identification and uptake by target cells. This precise targeting ability was also demonstrated in a mouse model, where the fluorescence intensity of SOD/PAC@CSF nanomotors in the hearts of IRI model mice was 10.2-fold that of the sham group and the fluorescence

intensity in the infarct and border zone (IRI region) was approximately twice as high as in the remote zone (healthy region), indicating effective targeting of the injured heart. In addition, the nanomotors that reached the injured part of the IRI heart could effectively restore the IRI heart of treatment by releasing NO, H₂S, and G-CSF within 48 h. For example, it improved LV systolic function (EF: 71.0%; FS: 39.8%), reduced infarct area (AAR/LV: 61.0%; AOI/LV: 13.0%; AOI/AAR: 21.4%), reduced the percentage of apoptotic cells (from 39.4% to 5.4%), lowered tissue CC3 protein expression, and helped return both ROS and inflammation levels to normal. This multifaceted and multistep strategy to intervene in the IRI process represents a promising therapeutic option for the effective treatment of IRI.

METHODS

Synthesis of SOD-Loaded Nanomotors. M-Arg, M-Cys, and diselenide cross-linker were prepared by drawing on previous literature.^{43,47} The detailed steps are available in the [Supporting Information](#).

N-Acryloyloxysuccinimide aqueous solution (1 mL, 0.2 mg mL⁻¹, 1.2 mmol) and G-CSF aqueous solution (0.1 mL, 1 mg mL⁻¹, 5.1 μmol) were mixed and reacted for 4 h at 4 °C in the dark.

M-Arg (42.0 mg, 0.16 mol), M-Cys (30.2 mg, 0.16 mol), and diselenide cross-linker (10.0 mg, 0.02 mol) were dissolved in 10 mL of ultrapure water, followed by the addition of the above double-bond-containing G-CSF (1.1 mL, 0.1 mg). After passing through N₂ for 30 min at room temperature, APS (1.6 mg, 2.0 wt %)-TEMED (3.2 mg, 4.0 wt %) was added to initiate the system and the reaction continued for 12 h. After the reaction, the system was dialyzed with an MDS00 dialysis membrane to remove the unreacted small molecules. After being freeze-dried, PAC@CSF was obtained.

Then, PAC@CSF was weighed at 10.0 mg each and ultrasonically dispersed in 10 mL of ultrapure water, then EDC (2.0 mg, 0.01 mmol) and NHS (1.2 mg, 0.01 mmol) were added in sequence to activate the carboxyl group for 3 h at room temperature. SOD (1.0 mg, 0.03 mmol) was then added, and the reaction was carried out at 4 °C for 12 h. After the reaction, the system was dialyzed with an MDS00 dialysis membrane to remove unreacted small molecules. Freeze-drying was used to obtain SOD/PAC@CSF nanomotors.

The preparation of cy5-NH₂ labeled SOD/PAC@CSF nanomotors was as follows: 10.0 mg of different samples were weighed and dispersed in 2 mL of ultrapure water (5 mg mL⁻¹), and then EDC (2.0 mg, 0.01 mmol) and NHS (1.2 mg, 0.01 mmol) were added sequentially to activate the carboxyl groups for 3 h at room temperature. Cy5-NH₂ (20 μL, 1 mg mL⁻¹ in DMSO) was then added, and the reaction was carried out overnight in the dark. After the reaction, the system was dialyzed with an MD1000 dialysis membrane to remove unreacted small molecules. Last, the cy5-NH₂ labeled SOD/PAC@CSF nanomotors were obtained by freeze-drying.

In addition, the preparation of SOD/PLY@CSF NPs, SOD/PA@CSF nanomotors, SOD/PC@CSF nanomotors, and the corresponding cy5-NH₂ labeled samples is available in the [Supporting Information](#).

Characterizations. The samples were placed on carbon support films and observed with a JM-2100 TRANSMISSION electron microscope (Hitachi) to obtain a TEM image. Samples were placed on nickel support films and observed by high angle annular dark field STEM to obtain mapping images. The zeta potential was recorded using a Zetasizer (Nano-Z, Malvern, UK). ¹H NMR spectra of the samples were recorded by using a Bruker Advance 400 spectrometer. Confocal laser scanning microscopy (CLSM, HP Apo TIRF 100X N.A. 1.49, Nikon, Ti-E-AIR, Japan) was used to obtain fluorescence images of the cells and tissue sections. The microplate reader (Multiskan FC, Thermo Fisher instrument Co., Ltd., US) was used to obtain absorbance data from the cell experiments. The movement behavior of the nanomotors was captured using an inverted

fluorescence microscope (MF53-N, Guangzhou Microshot Technology Co., Ltd., China).

Motion Capture and Analysis. H9c2 cells (1 × 10⁵ cells mL⁻¹) were inoculated into confocal dishes (Wuxi NEST Biotechnology Co., Ltd.) and cultured overnight. Prestimulated cells were obtained by stimulating the cells with LPS (1 μg mL⁻¹, Shanghai Yuanye Biotechnology Co., Ltd., S11060) for 24 h to distinguish them from normal cells. Cy5-labeled samples (20 μL, 1 mg mL⁻¹) were then added to the prestimulated and normal cell environments, respectively. The movement behavior of the nanomotors was recorded by inverted fluorescence microscopy (100× objective), and the movement trajectories were manually tracked using ImageJ software. Ten randomly selected particles were analyzed for their trajectories, and the mean velocity and velocity distribution histograms were calculated. In addition, the motor capacity of cy5-labeled SOD/PAC@CSF nanomotors in prestimulated H9c2 cells was evaluated over the different incubation times to assess the lifetime of the nanomotors.

Evaluation of the NO Production Capacity of Nanomotors. H9c2 cells (1 × 10⁵ cells mL⁻¹) were inoculated into confocal dishes and cultured overnight. After 3 h of hypoxia, the cells were cultured in normal medium containing different samples (200 μg mL⁻¹) for 24 h. Cells in the blank group were not treated. Cells were then stained with the NO probe DAF-FM DA and nuclei were labeled with Hoechst 33342. Fluorescence imaging was performed using CLSM (40× objective). Cellular fluorescence intensity was normalized using ImageJ software.

Evaluation of the H₂S Production Capacity of Nanomotors. H9c2 cells (1 × 10⁵ cells mL⁻¹) were inoculated into 6-well plates and cultured overnight. After 3 h of hypoxia, the cells were cultured in normal medium containing different samples (200 μg mL⁻¹) for 24 h. Cells in the blank group were not treated. The intracellular H₂S concentration was measured according to the protocol of the H₂S assay kit (Solarbio, BC2050).

Static Chemotaxis Behavior of Nanomotors in a Y-Shaped Channel. The static chemotaxis behavior of the nanomotors was observed using Y-shaped microchannels on a glass substrate ([Figure S14](#)). The main channel was 1 cm long and 0.4 cm wide, and the branch channel was 0.7 cm long and 0.3 cm wide. The concentration gradient of the chemotactic agent is established by the different cell lysates in the branch channel reservoir. Briefly, agarose (5 mg) was completely dissolved in PBS (500 μL) at 90 °C. The melted agarose was cooled to room temperature when 50 μL of LPS prestimulated H9c2 cell lysate was added and then transferred to 4 °C for curing, set as reservoir II-1; cured directly without the addition of cell lysate, set as reservoir II-2; and 50 μL of normal H9c2 cell lysate was added and then cured, set as reservoir III. Before assessing the chemotaxis of the nanomotors, the Y-shaped channels were pre-filled with a small amount of PBS, and then cy5-labeled nanomotors (50 μL) were gently dropped into reservoir I. Fluorescence images of reservoirs II and III were captured at 0, 10, 20, and 30 min using an inverted fluorescence microscope (Micro shot MF53-N, 10× objective). ImageJ software was used to normalize the fluorescence intensity.

Dynamic Chemotaxis Behavior of Nanomotors in a Microfluidic Channel. A three-entry, one-exit glass substrate microfluidic channel with dimensions of 2.2 cm (length) × 1.5 mm (width) × 300 μm (height) was used to assess the dynamic chemotaxis of nanomotors ([Figure S15](#)). Among them, LPS prestimulated H9c2 cell lysate dilution (lysate:PBS = 1:4, v/v) was buffer I; cy5-labeled sample in PBS was buffer II; normal H9c2 cell lysate dilution (lysate:PBS = 1:4, v/v) was buffer III-1; and PBS was buffer III-2. The flow rate was controlled at 0.6 mL h⁻¹. Video was captured continuously for 1 min (1 fps) using an inverted fluorescence microscope (10× objective) at a position near the exit. The fluorescence intensity perpendicular to the flow direction was measured using ImageJ software to analyze the chemotactic displacement of the nanomotors.

Cell Penetration of Nanomotors. Transwell chambers (24-well, 0.4 μm, Corning) were used to simulate different cell layers of cardiac tissue *in vitro* and thus to evaluate the permeability of cy5-labeled

samples ($200 \mu\text{g mL}^{-1}$) in different cell layers (Figure S17). HUVECs (0.2 mL , 1×10^5 cells) and H9c2 cells (0.6 mL , 1×10^5 cells) were inoculated and incubated overnight in the upper and lower chambers, respectively. After 3 h of hypoxia, normal medium containing different cy5-labeled samples ($200 \mu\text{g mL}^{-1}$) was added to the upper chamber and the upper chamber was transferred to the lower chamber and incubated for 24 h. Subsequently, the cell membrane was labeled with DiO and the nucleus was labeled with Hoechst 33342. Fluorescence imaging was performed using CLSM ($40\times$ objective). The fluorescence intensity was normalized using ImageJ software to analyze the penetration ability of the nanomotors.

Cellular Uptake Behavior. H9c2 cells (1×10^5 cells mL^{-1}) were inoculated into 6-well plates and cultured overnight. After 3 h of hypoxia, the cells were cultured in normal medium containing different cy5-labeled samples ($200 \mu\text{g mL}^{-1}$) for 24 h. Subsequently, the cell membrane was labeled with DiO and the nucleus was labeled with Hoechst 33342. Fluorescence imaging was performed using CLSM ($40\times$ objective). The fluorescence intensity was normalized using ImageJ software to analyze the uptake of nanomotors by the cells.

Cellular Uptake Pathways. To explore the main pathways of nanomotor entry into cells, H9c2 cells were treated with different inhibitors of endocytosis. H9c2 cells (1×10^5 cells mL^{-1}) were inoculated in 6-well plates and cultured until overnight. After 3 h of hypoxia, the cells were treated in normal medium containing chlorpromazine ($10 \mu\text{g mL}^{-1}$), nystatin ($15 \mu\text{g mL}^{-1}$), and cytochalasin D ($13.3 \mu\text{g mL}^{-1}$) or at $4 \text{ }^\circ\text{C}$ for 2 h, respectively. Then, the medium was abandoned, and the cells were incubated in inhibitor medium containing cy5-labeled SOD/PAC@CSF ($200 \mu\text{g mL}^{-1}$) for an additional 4 h. Subsequently, the cell membrane was labeled with DiO and the nucleus was labeled with Hoechst 33342. Fluorescence imaging was performed using CLSM ($40\times$ objective). The fluorescence intensity was normalized using ImageJ software analyze the uptake pathways of nanomotors by the cells.

Assessment of G-CSF Content. The G-CSF contents of PAC@CSF and SOD/PAC@CSF were determined according to the protocol of the Recombinant Mouse CSF (C-6His) kit (Novoprotein, P09920).

Assessment of SOD Activity. The enzyme activity of SOD was detected according to the operating protocol of the superoxide dismutase assay kit (Nanjing Jiancheng, A001-3).

In Vitro Degradation Characteristics. The SOD/PAC@CSF was dispersed in PBS and $650 \mu\text{M}$ H_2O_2 solution, respectively, to test the *in vitro* degradation performance of the nanomotors. The optical density ($\text{OD}_{660 \text{ nm}}$) of the mixture was measured within 48 h by using a UV-vis spectrophotometer.

Antiprotein Adhesion Properties. 2 mL of BSA-PBS solution (5 mg mL^{-1}) was pipetted, to which was added $20 \mu\text{L}$ of FITC solution (1 mg mL^{-1} in DMSO), and this was incubated for 12 h to obtain FITC-labeled BSA, which was mixed with cy5 labeled SOD/PAC@CSF for 4 h, and the particle size distribution of the mixed solution was measured using dynamic light scattering. Fluorescence imaging was performed using CLSM ($100\times$ objective).

Cell Culture. H9c2 rat myocardial cells and HL-1 mouse cardiac muscle cells (Shanghai Zhong Qiao Xin Zhou Biotechnology Co., Ltd.) were cultured in Dulbecco's modified Eagle's medium/HIGH GLUCOSE (with penicillin/streptomycin, Sperikon Life Science & Biotechnology Co., Ltd) with 10% fetal bovine serum (LONSERA, Shanghai Shuangru Biology Science & Technology Co., Ltd.). Human umbilical vein endothelial cells (HUVECs, Shanghai Xinyu Biotech Co., Ltd.) were cultured in medium containing 5% fetal bovine serum, 1% penicillin/streptomycin and 1% endothelial growth factor. All cells were cultured at $37 \text{ }^\circ\text{C}$ in a humidified environment with 5% CO_2 .

Hypoxic-Reoxygenation Injured Cell Model. Cells were treated with sugar-free DMEM medium and incubated in a hypoxic incubator (Mitsubishi Gas Chemical Company, AnaeroPack, $\leq 0.1\%$ O_2) at $37 \text{ }^\circ\text{C}$ for 3 h, followed by 24 h in a standard incubator with a normal atmosphere (5% CO_2 , 95% O_2 , $37 \text{ }^\circ\text{C}$) to simulate ischemia-reperfusion injury. Drug therapy was administered at the start of reoxygenation.

Cascade Effect of Nanomotors for Relieving Oxidative Stress and Releasing NO. H9c2 cells (1×10^5 cells mL^{-1}) were inoculated in 6-well plates and cultured until overnight. After 3 h of hypoxia, the cells were cultured in normal medium containing different samples (SOD: $20 \mu\text{g mL}^{-1}$, M-Arg: $84 \mu\text{g mL}^{-1}$, PAC@CSF: $180 \mu\text{g mL}^{-1}$ and SOD/PAC@CSF: $200 \mu\text{g mL}^{-1}$) for 24 h. The cells in the blank group were not treated. The intracellular $\text{O}_2^{\bullet-}$ and H_2O_2 concentration were measured according to the protocol of the $\text{O}_2^{\bullet-}$ assay kit (Solarbio, BC1295) and the H_2O_2 assay kit (Beyotime, S0038), respectively. Cells are cultured by a similar process. The intracellular NO was measured according to the protocol of the NO Assay Kit (Beyotime, S0021S) after treated with different samples ($200 \mu\text{g mL}^{-1}$) for 24h.

Nanomotors Scavenge ROS in Vitro. H9c2 cells (1×10^5 cells mL^{-1}) were inoculated in confocal dishes and cultured until overnight. After 3 h of hypoxia, the cells were cultured in normal medium containing different samples ($200 \mu\text{g mL}^{-1}$) for 24 h. The cells in the blank group were not treated. Subsequently, cells were stained with the ROS probe DCFH-DA and nuclei were labeled with Hoechst 33342. Fluorescence imaging was performed using CLSM ($20\times$ objective). Cellular fluorescence intensity was normalized using ImageJ software.

Nanomotors Reduce Proinflammatory Factors in Vitro. HL-1 cells (1×10^5 cells mL^{-1}) were inoculated in 96-well plates and cultured until overnight. After 3 h of hypoxia, the cells were cultured in normal medium containing different samples ($200 \mu\text{g mL}^{-1}$) for 24 h. The cells in the blank group were not treated. The supernatant was collected, and IL-6 and TNF- α concentrations were assayed according to the protocols of the IL-6 Assay Kit (MEIMIAN, ELISA, MM-0163M2) and the TNF- α Assay Kit (MEIMIAN, ELISA, MM0132M2), respectively.

Nanomotors Mitigate Calcium Overload. H9c2 cells (1×10^5 cells mL^{-1}) were inoculated in confocal dishes and cultured until overnight. After 3 h of hypoxia, the cells were cultured in normal medium containing different samples ($200 \mu\text{g mL}^{-1}$) for 24 h. The cells in the blank group were not treated. Subsequently, cells were stained with the Ca^{2+} probe Flou-4 AM and nuclei were labeled with Hoechst 33342. Fluorescence imaging was performed using CLSM ($100\times$ objective). Cellular fluorescence intensity was normalized using ImageJ software.

Cell Viability Assays. To assess the biocompatibility of the nanomotors, H9c2 cells (5×10^4 cells mL^{-1}) were inoculated in 96-well plates and cultured overnight. The medium was removed, and $150 \mu\text{L}$ of culture medium containing different samples was added to each well separately and incubated for 24 h. Each well was then repeated three times. Subsequently, $20 \mu\text{L}$ of MTT (5 mg mL^{-1}) was added and incubated for 4 h. Cell viability was determined by measuring the absorbance at 570 nm by the microplate reader. Similar protocols were applied to determine cell viability assays of different concentrations of SOD/PAC@CSF and different incubation times of SOD/PAC@CSF, except that different concentrations or different incubation times of SOD/PAC@CSF were used instead of different samples. Similarly, to compare the *in vitro* treatment effects of different samples, H9c2 cells (5×10^4 cells mL^{-1}) were inoculated in 96-well plates and incubated overnight. After 3 h of hypoxia, cell viability was assayed for different samples, different SOD/PAC@CSF nanomotor concentrations, and different incubation times in a similar experimental procedure.

Western Blot Analysis. Total proteins were extracted using RIPA lysates (Beyotime China, P0013B) containing 1% protease inhibitor cocktail (Beyotime China, P1005). The proteins were separated by an SDS-PAGE gel and then transferred to PVDF membranes. After incubation in 5% BSA blocking buffer for 60 min, the membranes were incubated overnight at $4 \text{ }^\circ\text{C}$ with primary antibodies (Cleaved Caspase-3 Rabbit mAb, CST, #9664, 1:1000; β -Actin Mouse mAb, CST, #3700, 1:1000). Thereafter, the membranes were incubated with corresponding HRP-conjugated IgG secondary antibodies (HRP-labeled Goat Anti-Rabbit IgG (H+L), WELLBi Shanghai, WB2177, 1:5000; HRP-labeled Goat Anti-Mouse IgG (H+L), WELLBi Shanghai, WB3176, 1:5000) for 1 h at room temperature.

Protein bands were detected by a digital chemiluminescence system (Bio-Rad USA) and normalized using the ImageJ software.

Ischemia-Reperfusion Injury Mouse Model. C57BL/6 mice (male, 6–8 weeks old) were purchased from Shanghai SLAC Laboratory Animal Co. Ltd. (Shanghai, China). Eight-week-old mice were anesthetized with 2% isoflurane in the induction chamber. The third and fourth intercostal spaces were exposed by blunt dissection, and the heart was externalized after the intercostal space was enlarged with mosquito forceps. Then the left anterior descending (LAD) coronary artery was ligated with a 6–0 suture to induce myocardial ischemia. The ischemic state was maintained for 45 min, after which the suture was released to allow reperfusion for 48 h. Drug therapy was administered at the 0 and 24 h of reperfusion.

In Vivo Imaging. Cy5-labeled SOD/PAC@CSF nanomotors and cy5-labeled SOD/PLY@CSF (100 μL , 2 mg mL^{-1}) were injected into normal or IRI mice through the tail vein. Six h later, the mice were executed to remove the major organs, and the enrichment of samples in the organs was monitored by an *in vivo* imaging system (IVIS Spectrum, PerkinElmer).

Biodistribution. Cy5-labeled SOD/PAC@CSF nanomotors and cy5-labeled SOD/PLY@CSF (100 μL , 2 mg mL^{-1}) were injected into normal or IRI mice through the tail vein. After a certain period of time, the mice were executed to remove the major organs and the organs were lysed and ground for homogenization. The fluorescence intensity in the supernatant was measured by centrifugal separation. The percentage of the injected dose per gram of tissue (% ID/g) was calculated.

Targeting Effects of Nanomotors in Cardiac Tissue. Cy5-labeled SOD/PAC@CSF nanomotors and cy5-labeled SOD/PLY@CSF (100 μL , 2 mg mL^{-1}) were injected into normal or IRI mice through the tail vein. After a period of time, the hearts were removed and frozen into sections (divided into three parts, remote zone, infarct zone, and border zone, with the infarct zone representing the ligated area). The sections were scanned using CLSM (10 \times objective). ImageJ software was used to analyze the fluorescence intensity.

Penetration of Nanomotors in Cardiac Tissue. Cy5-labeled SOD/PAC@CSF nanomotors and cy5-labeled SOD/PLY@CSF (100 μL , 2 mg mL^{-1}) were injected into normal or IRI mice through the tail vein. Six hours later, hearts were removed, and cryosections were performed along the middle. Sections were stained with rabbit antimouse CD31 antibody (Servicebio, GB112151, 1:200), goat antirabbit Alexa Fluor 488 (Servicebio, GB25303, 1:200), DAPI (Beyotime, C1006). Subsequently, the sections were scanned with a tissue scanner Panoramic MIDI (3D HISTECH, Hungary) and processed with Panoramic viewer software. ImageJ software was used to analyze the fluorescence intensity.

Pharmacokinetic Analysis. SOD/PAC@CSF nanomotors (800 μL , 2 mg mL^{-1}) and pure G-CSF (800 μL , 0.0175 $\mu\text{g mL}^{-1}$) were injected into SD rats via the tail vein. At the indicated time points after injection (0.12, 1, 3, 6, 12, 24, 36, and 48 h), approximately 500 μL of blood was removed from the eye sockets of the rats, and the supernatant was extracted by centrifugation and analyzed according to the operating protocol of the Recombinant Mouse CSF (C-6His) kit (Novoprotein, P09920) to detect the level of G-CSF.

In Vivo Therapeutic Effect Study. PBS (IRI), G-CSF (100 $\mu\text{g kg}^{-1}$), SOD/PAC (114 μL , 2 mg mL^{-1}), SOD/PLY@CSF (114 μL , 2 mg mL^{-1}), and SOD/PAC@CSF (114 μL , 2 mg mL^{-1}) were injected into IRI mice at 0 and 24 h, respectively, and untreated mice were used as the sham group. After 48 h, echocardiography analysis was performed. Subsequently, mice were executed and hearts were collected for Evans blue and triphenyltetrazolium chloride (TTC), terminal deoxynucleotidyl transferase dUTP nick end labeling (TUNEL) assay, and analyze the changes of cleaved caspase3 (CC3), ROS, IL-6 and TNF- α levels during the treatment.

Echocardiography Analysis. Echocardiography was carried out 48 h after reperfusion. The parasternal long-axis views of the heart were obtained with the RMV 2100 scan head on a Vevo 2100 (VisualSonics Inc., Toronto, Canada) in mice anesthetized with 2% isoflurane. Heart rate should be maintained above 400 bpm. Ejection

fraction (EF) and fraction shortening (FS) were measured in M-mode images.

Evans Blue and Triphenyltetrazolium Chloride (TTC) Staining. At the end of reperfusion, we ligated the LAD again with a 6–0 silk suture along the original trace and then injected Evans blue (Solarbio China, E8010) until the dye was visible in the remote region of the heart. After freezing at $-20\text{ }^{\circ}\text{C}$ for 20 min, the heart was then cut into four pieces. Slices were incubated at 1%TTC (Solarbio China, T8170) at $37\text{ }^{\circ}\text{C}$ for 20 min and transferred to 4% paraformaldehyde to be fixed overnight. We took pictures with a digital camera, which were normalized by ImageJ software.

Terminal Deoxynucleotidyl Transferase dUTP Nick End Labeling (TUNEL) Assay. The experiment was carried out on frozen sections according to the assay kit (Beyotime China, C1090) instruction. And the nucleus was labeled with DAPI (Servicebio, G1012). Fluorescence images were obtained by CLSM (50 \times objective). TUNEL-positive cells are considered to be apoptotic cells. The apoptotic cell ratio was calculated as the number of apoptotic cells to total nucleus.

ROS Immunofluorescence Staining. SOD/PAC@CSF nanomotors (114 μL , 2 mg mL^{-1}) were injected into IRI mice through the tail vein. Six and 48 h later, hearts were removed and cryosections were performed along the middle. Sections were stained with ROS staining solution (Sigma, D7008) and DAPI (Servicebio, G1012). Subsequently, the sections were scanned with a tissue scanner panoramic MIDI and processed with panoramic viewer software. ImageJ software was used to analyze the fluorescence intensity.

IL-6 and TNF- α Immunofluorescence Staining. SOD/PAC@CSF nanomotors (114 μL , 2 mg mL^{-1}) were injected into IRI mice through the tail vein. Six hours and 48 h later, hearts were removed and cryosections were performed along the middle. Sections were stained with recombinant rabbit antimouse IL-6 antibody (Abcam, EPR23819–103, ab290735, 1:100), recombinant rabbit antimouse Anti-TNF alpha antibody (Abcam, RM1005, ab307164, 1:1000), goat antirabbit IgG H&L (Abcam, ab6712, 1:100), TAS-488 and TAS-555 tyramine conversion reagent (Biomed word, Shanghai, 1:100). Subsequently, the sections were scanned with CLSM (10 \times objective). ImageJ software was used to analyze the fluorescence intensity.

Statistical Analysis. All data are presented as means with standard errors. Statistical difference was evaluated using Student's *t* test and the statistical difference in different groups via one-way ANOVA.

Ethical Statement. All animal experiments were performed under the guidelines of the Animal Care Committee of Nanjing Normal University (IACUC-20201101–1, Nanjing, China).

ASSOCIATED CONTENT

Supporting Information

The Supporting Information is available free of charge at <https://pubs.acs.org/doi/10.1021/acsnano.3c02781>.

Additional experimental procedures including materials, synthesis of M-Arg (*N*-methacryl-L-arginine), M-Cys (*N*-methacryloyl-L-cysteine), diselenide cross-linker, poly-*N*-methacrylate-arginine-encapsulated G-CSF (PA@CSF), poly-*N*-methacrylate-cysteine-encapsulated G-CSF (PC@CSF), poly-*N*-methacrylate-lysine-encapsulated G-CSF (PLY@CSF), SOD-loaded nanomotors and cy5-NH₂ labeled samples; Figures S1–S35; Tables S1–S3; Supporting References (PDF)

Movie S1: Motion behavior of SOD/PLY@CSF in normal H9c2 cells environment for 20 s (MP4)

Movie S2: Motion behavior of SOD/PA@CSF in normal H9c2 cells environment for 20 s (MP4)

Movie S3: Motion behavior of SOD/PC@CSF in normal H9c2 cells environment for 20 s (MP4)

Movie S4: Motion behavior of SOD/PAC@CSF in normal H9c2 cells environment for 20 s (MP4)

Movie S5: Motion behavior of SOD/PLY@CSF in prestimulated H9c2 cells environment for 20 s (MP4)
Movie S6: Motion behavior of SOD/PA@CSF in prestimulated H9c2 cells environment for 20 s (MP4)
Movie S7: Motion behavior of SOD/PC@CSF in prestimulated H9c2 cells environment for 20 s (MP4)
Movie S8: Motion behavior of SOD/PAC@CSF in prestimulated H9c2 cells environment for 20 s (MP4)
Movie S9: Motion behavior of SOD/PAC@CSF after incubation with prestimulated H9c2 cells for different time (MP4)

AUTHOR INFORMATION

Corresponding Authors

Yuxiang Dai – Department of Cardiology, Zhongshan Hospital, Fudan University, Shanghai Institute of Cardiovascular Diseases, National Clinical Research Center for Interventional Medicine, Shanghai 200433, China; Email: dai.yuxiang@hotmail.com

Chun Mao – National and Local Joint Engineering Research Center of Biomedical Functional Materials, School of Chemistry and Materials Science, Nanjing Normal University, Nanjing 210023, China; orcid.org/0000-0003-4085-3414; Email: maochun@njnu.edu.cn

Mimi Wan – National and Local Joint Engineering Research Center of Biomedical Functional Materials, School of Chemistry and Materials Science, Nanjing Normal University, Nanjing 210023, China; orcid.org/0000-0002-8686-7961; Email: wanmimi@njnu.edu.cn

Authors

Nan Li – National and Local Joint Engineering Research Center of Biomedical Functional Materials, School of Chemistry and Materials Science, Nanjing Normal University, Nanjing 210023, China

Chenxing Huang – Department of Cardiology, Zhongshan Hospital, Fudan University, Shanghai Institute of Cardiovascular Diseases, National Clinical Research Center for Interventional Medicine, Shanghai 200433, China

Jie Zhang – Department of Radiology, Shanghai General Hospital, Shanghai Jiao Tong University School of Medicine, Shanghai 200025, China

Junyue Zhang – National and Local Joint Engineering Research Center of Biomedical Functional Materials, School of Chemistry and Materials Science, Nanjing Normal University, Nanjing 210023, China

Jia Huang – Department of Cardiology, Zhongshan Hospital, Fudan University, Shanghai Institute of Cardiovascular Diseases, National Clinical Research Center for Interventional Medicine, Shanghai 200433, China

Shangshang Li – National and Local Joint Engineering Research Center of Biomedical Functional Materials, School of Chemistry and Materials Science, Nanjing Normal University, Nanjing 210023, China

Xue Xia – National and Local Joint Engineering Research Center of Biomedical Functional Materials, School of Chemistry and Materials Science, Nanjing Normal University, Nanjing 210023, China

Ziyu Wu – National and Local Joint Engineering Research Center of Biomedical Functional Materials, School of Chemistry and Materials Science, Nanjing Normal University, Nanjing 210023, China

Chenglong Chen – National and Local Joint Engineering Research Center of Biomedical Functional Materials, School of Chemistry and Materials Science, Nanjing Normal University, Nanjing 210023, China

Shuwan Tang – National and Local Joint Engineering Research Center of Biomedical Functional Materials, School of Chemistry and Materials Science, Nanjing Normal University, Nanjing 210023, China

Xiangyu Xiao – National and Local Joint Engineering Research Center of Biomedical Functional Materials, School of Chemistry and Materials Science, Nanjing Normal University, Nanjing 210023, China

Hui Gong – Department of Cardiology, Zhongshan Hospital, Fudan University, Shanghai Institute of Cardiovascular Diseases, National Clinical Research Center for Interventional Medicine, Shanghai 200433, China

Complete contact information is available at:
<https://pubs.acs.org/10.1021/acsnano.3c02781>

Author Contributions

[†]N.L., C.H., and J.Z. contributed equally.

Notes

The authors declare no competing financial interest.

ACKNOWLEDGMENTS

The work was supported by National Natural Science Foundation of China (No. 22175096, 22275095), Jiangsu Key Laboratory of Biofunctional Materials, Jiangsu Collaborative Innovation Center of Biomedical Functional Materials, the Qinglan Project Foundation of Colleges and Universities of Jiangsu Province, the Postgraduate Research & Practice Innovation Program of Jiangsu Province (No. KYCX22_1545) and the Priority Academic Program Development of Jiangsu Higher Education Institution, Clinical Research Plan of Shanghai Hospital Development Center (No. SHDC2020CR1007A), Program of Shanghai Academic Research Leader (No. 22XD1423300), Natural Science Foundation of Shanghai (No. 20ZR1439700).

REFERENCES

- Heusch, G. Myocardial Ischaemia-Reperfusion Injury and Cardioprotection in Perspective. *Nat. Rev. Cardiol.* **2020**, *17*, 773–789.
- Reed, G. W.; Rossi, J. E.; Cannon, C. P. Acute Myocardial Infarction. *Lancet* **2017**, *389*, 197–210.
- Kingery, J. R.; Hamid, T.; Lewis, R. K.; Ismahil, M. A.; Bansal, S. S.; Rokosh, G.; Townes, T. M.; Ildstad, S. T.; Jones, S. P.; Prabhu, S. D. Leukocyte iNOS is Required for Inflammation and Pathological Remodeling in Ischemic Heart Failure. *Basic Res. Cardiol.* **2017**, *112*, 19.
- Jia, L.; Wang, Y.; Wang, Y.; Ma, Y.; Shen, J.; Fu, Z.; Wu, Y.; Su, S. a.; Zhang, Y.; Cai, Z.; Wang, J. a.; Xiang, M. Heme Oxygenase-1 in Macrophages Drives Septic Cardiac Dysfunction via Suppressing Lysosomal Degradation of Inducible Nitric Oxide Synthase. *Circ. Res.* **2018**, *122*, 1532–1544.
- Mungrue, I. N.; Gros, R.; You, X.; Pirani, A.; Azad, A.; Csont, T.; Schulz, R.; Butany, J.; Stewart, D. J.; Husain, M. Cardiomyocyte Overexpression of iNOS In Mice Results in Peroxynitrite Generation, Heart Block, and Sudden Death. *J. Clin. Invest.* **2002**, *109*, 735–743.
- Darra, E.; Rungtatscher, A.; de Prati, A. C.; Podesser, B. K.; Faggian, G.; Scarabelli, T.; Mazzucco, A.; Hallström, S.; Suzuki, H. Dual Modulation of Nitric Oxide Production in the Heart During Ischaemia/Reperfusion Injury and Inflammation. *Thromb. Haemost.* **2010**, *104*, 200–206.

- (7) Valko, M.; Leibfritz, D.; Moncol, J.; Cronin, M. T. D.; Mazur, M.; Telser, J. Free Radicals and Antioxidants in Normal Physiological Functions and Human Disease. *Int. J. of Biochem. Cell* **2007**, *39*, 44–84.
- (8) Lugin, J.; Rosenblatt-Velin, N.; Parapanov, R.; Liaudet, L. The Role of Oxidative Stress During Inflammatory Processes. *Biol. Chem.* **2014**, *395*, 203–230.
- (9) Ibanez, B.; Heusch, G.; Ovize, M.; Van de Werf, F. Evolving Therapies for Myocardial Ischemia/Reperfusion Injury. *J. Am. Coll. Cardiol.* **2015**, *65*, 1454–1471.
- (10) Heusch, G.; Gersh, B. J. The Pathophysiology of Acute Myocardial Infarction and Strategies of Protection Beyond Reperfusion: a Continual Challenge. *Eur. Heart J.* **2016**, *38*, 774–784.
- (11) Davidson, S. M.; Ferdinandy, P.; Andreadou, I.; Bøtker, H. E.; Heusch, G.; Ibáñez, B.; Ovize, M.; Schulz, R.; Yellon, D. M.; Hausenloy, D. J.; Garcia-Dorado, D. Multitarget Strategies to Reduce Myocardial Ischemia/Reperfusion Injury. *J. Am. Coll. Cardiol.* **2019**, *73*, 89–99.
- (12) Tani, M.; Neely, J. R. Role of Intracellular Na⁺ in Ca²⁺ Overload and Depressed Recovery of Ventricular Function of Reperfused Ischemic Rat Hearts. Possible Involvement of H⁺-Na⁺ and Na⁺-Ca²⁺ Exchange. *Circ. Res.* **1989**, *65*, 1045–1056.
- (13) Hausenloy, D. J.; Yellon, D. M. Myocardial Ischemia-Reperfusion Injury: a Neglected Therapeutic Target. *J. Clin. Invest.* **2013**, *123*, 92–100.
- (14) Wang, R.; Wang, M.; He, S.; Sun, G.; Sun, X. Targeting Calcium Homeostasis in Myocardial Ischemia/Reperfusion Injury: An Overview of Regulatory Mechanisms and Therapeutic Reagents. *Front. Pharmacol.* **2020**, *11*, 872.
- (15) Németh, T.; Sperandio, M.; Mócsai, A. Neutrophils as Emerging Therapeutic Targets. *Nat. Rev. Drug Discovery* **2020**, *19*, 253–275.
- (16) Hori, M.; Nishida, K. Oxidative Stress and Left Ventricular Remodelling after Myocardial Infarction. *Cardiovasc. Res.* **2008**, *81*, 457–464.
- (17) Chouchani, E. T.; Pell, V. R.; James, A. M.; Work, L. M.; Saeb-Parsy, K.; Frezza, C.; Krieg, T.; Murphy, M. P. A Unifying Mechanism for Mitochondrial Superoxide Production during Ischemia-Reperfusion Injury. *Cell Metab.* **2016**, *23*, 254–263.
- (18) Zhao, T.; Wu, W.; Sui, L.; Huang, Q.; Nan, Y.; Liu, J.; Ai, K. Reactive Oxygen Species-Based Nanomaterials for the Treatment of Myocardial Ischemia Reperfusion Injuries. *Bioact. Mater.* **2022**, *7*, 47–72.
- (19) Zhang, G.; Gao, S.; Li, X.; Zhang, L.; Tan, H.; Xu, L.; Chen, Y.; Geng, Y.; Lin, Y.; Aertker, B.; Sun, Y. Pharmacological Postconditioning with Lactic Acid and Hydrogen Rich Saline Alleviates Myocardial Reperfusion Injury in Rats. *Sci. Rep.* **2015**, *5*, 9858.
- (20) Bland, A. R.; Payne, F. M.; Ashton, J. C.; Jamialahmadi, T.; Sahebkar, A. The Cardioprotective Actions of Statins in Targeting Mitochondrial Dysfunction Associated with Myocardial Ischaemia-Reperfusion Injury. *Pharmacol. Res.* **2022**, *175*, 105986.
- (21) Yebo, H. G.; Aschmann, H. E.; Puhon, M. A. Finding the Balance Between Benefits and Harms When Using Statins for Primary Prevention of Cardiovascular Disease. *Ann. Int. Med.* **2019**, *170*, 1–10.
- (22) Igarashi, N.; Nozawa, T.; Fujii, N.; Suzuki, T.; Matsuki, A.; Nakadate, T.; Igawa, A.; Inoue, H. Influence of β -Adrenoceptor Blockade on the Myocardial Accumulation of Fatty Acid Tracer and Its Intracellular Metabolism in the Heart After Ischemia-Reperfusion Injury. *Circ. J.* **2006**, *70*, 1509–1514.
- (23) Lobo Gonzalez, M.; Galan Arriola, C.; Vilchez-Tschischke, J. P.; Lopez, G. J.; Gavilan-Santiago, M.; Fernandez-Jimenez, R.; Pizarro, G. J.; Sanchez-Gonzalez, J. P.; Ibanez, B. P6423Cardioprotective Effect of Metoprolol in Myocardial Ischemic/Reperfusion Injury: the Role of Total Ischemic Time. *Eur. Heart J.* **2019**, *40*, No. ehz746.1017.
- (24) Ma, H.; Gong, H.; Chen, Z.; Liang, Y.; Yuan, J.; Zhang, G.; Wu, J.; Ye, Y.; Yang, C.; Nakai, A.; Komuro, I.; Ge, J.; Zou, Y. Association of Stat3 with HSF1 Plays a Critical Role in G-CSF-Induced Cardio-Protection Against Ischemia/Reperfusion Injury. *J. Mol. Cell. Cardiol.* **2012**, *52*, 1282–1290.
- (25) Ince, H.; Petzsch, M.; Kleine, H. D.; Schmidt, H.; Rehders, T.; Körber, T.; Schümichen, C.; Freund, M.; Nienaber, C. A. Preservation From Left Ventricular Remodeling by Front-Integrated Revascularization and Stem Cell Liberation in Evolving Acute Myocardial Infarction by Use of Granulocyte-Colony-Stimulating Factor (FIRST-LINE-AMI). *Circulation* **2005**, *112*, 3097–3106.
- (26) Takano, H.; Ueda, K.; Hasegawa, H.; Komuro, I. G-CSF Therapy for Acute Myocardial Infarction. *Trends Pharmacol. Sci.* **2007**, *28*, 512–517.
- (27) Lozano, O.; Torres-Quintanilla, A.; García-Rivas, G. Nanomedicine for the Cardiac Myocyte: Where are We? *J. Controlled Release* **2018**, *271*, 149–165.
- (28) Cashman, N.; Tan, L.-Y.; Krieger, C.; Mädler, B.; Mackay, A.; Mackenzie, I.; Benny, B.; Nantel, S.; Fabros, M.; Shinobu, L.; Yousefi, M.; Eisen, A. Pilot Study of Granulocyte Colony Stimulating Factor (G-CSF)-Mobilized Peripheral Blood Stem Cells in Amyotrophic Lateral Sclerosis (ALS). *Muscle Nerve* **2008**, *37*, 620–625.
- (29) Dawn, B.; Guo, Y.; Rezaadeh, A.; Huang, Y.; Stein, A. B.; Hunt, G.; Tiwari, S.; Varma, J.; Gu, Y.; Prabhu, S. D.; Kajstura, J.; Anversa, P.; Ildstad, S. T.; Bolli, R. Postinfarct Cytokine Therapy Regenerates Cardiac Tissue and Improves Left Ventricular Function. *Circ. Res.* **2006**, *98*, 1098–1105.
- (30) Abdel-Latif, A.; Bolli, R.; Zuba-Surma, E. K.; Tleyjeh, I. M.; Hornung, C. A.; Dawn, B. Granulocyte Colony-Stimulating Factor Therapy for Cardiac Repair after Acute Myocardial Infarction: A Systematic Review and Meta-Analysis of Randomized Controlled Trials. *Am. Heart J.* **2008**, *156*, 216–226.
- (31) Tanaka, H.; Satake-Ishikawa, R.; Ishikawa, M.; Matsuki, S.; Asano, K. Pharmacokinetics of Recombinant Human Granulocyte Colony-stimulating Factor Conjugated to Polyethylene Glycol in Rats. *Cancer Res.* **1991**, *51*, 3710–3714.
- (32) Gibaud, S.; Rousseau, C.; Weingarten, C.; Favier, R.; Douay, L.; Andreux, J. P.; Couvreur, P. Polyalkylcyanoacrylate Nanoparticles as Carriers for Granulocyte-Colony Stimulating Factor (G-CSF). *J. Controlled Release* **1998**, *52*, 131–139.
- (33) Margulis, K.; Honkala, A.; Kalashnikova, I.; Noll, S. E.; Hill, M.; Zare, R. N.; Smith, B. R. Nanoparticles Decorated with Granulocyte-Colony Stimulating Factor for Targeting Myeloid Cells. *Nanoscale* **2020**, *12*, 2752–2763.
- (34) Lv, Q.; Cheng, L.; Lu, Y.; Zhang, X.; Wang, Y.; Deng, J.; Zhou, J.; Liu, B.; Liu, J. Thermosensitive Exosome-Liposome Hybrid Nanoparticle-Mediated Chemotherapy for Improved Treatment of Metastatic Peritoneal Cancer. *Adv. Sci.* **2020**, *7*, 2000515.
- (35) Shin, M.; Lee, H.-A.; Lee, M.; Shin, Y.; Song, J.-J.; Kang, S.-W.; Nam, D.-H.; Jeon, E. J.; Cho, M.; Do, M.; Park, S.; Lee, M. S.; Jang, J.-H.; Cho, S.-W.; Kim, K.-S.; Lee, H. Targeting Protein and Peptide Therapeutics to the Heart via Tannic Acid Modification. *Nat. Biomed. Eng.* **2018**, *2*, 304–317.
- (36) Li, C.; Hu, M.; Wang, Y.; Lu, H.; Deng, J.; Yan, X. Hydrogen Sulfide Preconditioning Protects Against Myocardial Ischemia/Reperfusion Injury in Rats through Inhibition of Endo/Sarcoplasmic Reticulum Stress. *Int. J. Clin. Exp. Pathol.* **2015**, *8*, 7740–51.
- (37) Calabrese, V.; Mancuso, C.; Calvani, M.; Rizzarelli, E.; Butterfield, D. A.; Giuffrida Stella, A. M. Nitric Oxide in the Central Nervous System: Neuroprotection Versus Neurotoxicity. *Nat. Rev. Neurosci.* **2007**, *8*, 766–775.
- (38) Li, T.; Liu, Z.; Hu, J.; Chen, L.; Chen, T.; Tang, Q.; Yu, B.; Zhao, B.; Mao, C.; Wan, M. A Universal Chemotactic Targeted Delivery Strategy for Inflammatory Diseases. *Adv. Mater.* **2022**, *34*, 2206654.
- (39) Xie, Z. Z.; Liu, Y.; Bian, J. S. Hydrogen Sulfide and Cellular Redox Homeostasis. *Oxid. Med. Cell. Longev.* **2016**, 6043038.
- (40) Wang, W. L.; Ge, T. Y.; Chen, X.; Mao, Y.; Zhu, Y. Z. Advances in the Protective Mechanism of NO, H₂S, and H₂ in Myocardial Ischemic Injury. *Front. Cardiovasc. Med.* **2020**, *7*, 588206.
- (41) Ding, H.; Chang, J.; He, F.; Gai, S.; Yang, P. Hydrogen Sulfide: An Emerging Precision Strategy for Gas Therapy. *Adv. Healthc. Mater.* **2022**, *11*, 2101984.

- (42) Rickover, O.; Zinman, T.; Kaplan, D.; Shainberg, A. Exogenous Nitric Oxide Triggers Classic Ischemic Preconditioning by Preventing Intracellular Ca^{2+} Overload in Cardiomyocytes. *Cell Calcium* **2008**, *43*, 324–333.
- (43) Queen, L. R.; Ferro, A. β -Adrenergic Receptors and Nitric Oxide Generation in the Cardiovascular System. *Cell. Mol. Life Sci.* **2006**, *63*, 1070–1083.
- (44) Kim, Y.; Binauld, S.; Stenzel, M. H. Zwitterionic Guanidine-Based Oligomers Mimicking Cell-Penetrating Peptides as a Nontoxic Alternative to Cationic Polymers to Enhance the Cellular Uptake of Micelles. *Biomacromolecules* **2012**, *13*, 3418–3426.
- (45) Huang, X.; Huang, Y. Solubilization of Organic Compounds by Arginine-Derived Polymers. *Chin. Chem. Lett.* **2015**, *26*, 636–640.
- (46) Tang, X.; Chen, L.; Wu, Z.; Li, Y.; Zeng, J.; Jiang, W.; Lv, W.; Wan, M.; Mao, C.; Zhou, M. Lipophilic NO-Driven Nanomotors as Drug Balloon Coating for the Treatment of Atherosclerosis. *Small* **2023**, *19*, 2203238.
- (47) Garipcan, B.; Andaç, M.; Uzun, L.; Denizli, A. Methacryloyl-lamidocysteine Functionalized Poly(2-hydroxyethyl methacrylate) Beads and Its Design as a Metal-Chelate Affinity Support for Human Serum Albumin Adsorption. *React. Funct. Polym.* **2004**, *59*, 119–128.
- (48) Tian, Y.; Zheng, J.; Tang, X.; Ren, Q.; Wang, Y.; Yang, W. Near-Infrared Light-Responsive Nanogels with Diselenide-Cross-Linkers for On-Demand Degradation and Triggered Drug Release. *Part. Part. Syst. Char.* **2015**, *32*, 547–551.
- (49) Davignon, J.; Ganz, P. Role of Endothelial Dysfunction in Atherosclerosis. *Circulation* **2004**, DOI: 10.1161/01.CIR.0000131515.03336.f8.
- (50) Park, H. S.; Jung, H. Y.; Park, E. Y.; Kim, J.; Lee, W. J.; Bae, Y. S. Cutting Edge: Direct Interaction of TLR4 with NAD(P)H Oxidase 4 Isozyme Is Essential for Lipopolysaccharide-Induced Production of Reactive Oxygen Species and Activation of NF- κ B. *J. Immunol.* **2004**, *173*, 3589–3593.
- (51) Liang, Z.; Tu, Y.; Peng, F. Polymeric Micro/Nanomotors and Their Biomedical Applications. *Adv. Healthc. Mater.* **2021**, *10*, 2100720.
- (52) Tu, Y.; Peng, F.; Wilson, D. A. Motion Manipulation of Micro- and Nanomotors. *Adv. Mater.* **2017**, *29*, 1701970.
- (53) Liang, H.; Peng, F.; Tu, Y. Active Therapy Based on the Byproducts of Micro/Nanomotors. *Nanoscale* **2023**, *15*, 953–962.
- (54) Cao, D.; Tian, S.; Huang, H.; Chen, J.; Pan, S. Divalent Folate Modification on PEG: An Effective Strategy for Improving the Cellular Uptake and Targetability of PEGylated Polyamidoamine-Polyethylenimine Copolymer. *Mol. Pharmaceut.* **2015**, *12*, 240–252.
- (55) Zhang, X.; Xu, X.; Li, Y.; Hu, C.; Zhang, Z.; Gu, Z. Virion-Like Membrane-Breaking Nanoparticles with Tumor-Activated Cell-and-Tissue Dual-Penetration Conquer Impermeable Cancer. *Adv. Mater.* **2018**, *30*, 1707240.
- (56) Chen, Z.; Xia, T.; Zhang, Z.; Xie, S.; Wang, T.; Li, X. Enzyme-Powered Janus Nanomotors Launched from Intratumoral Depots to Address Drug Delivery Barriers. *Chem. Eng. J.* **2019**, *375*, 122109.
- (57) Chen, H.; Shi, T.; Wang, Y.; Liu, Z.; Liu, F.; Zhang, H.; Wang, X.; Miao, Z.; Liu, B.; Wan, M.; Mao, C.; Wei, J. Deep Penetration of Nano-level Drugs and Micrometer-Level T Cells Promoted by Nanomotors for Cancer Immunotherapy. *J. Am. Chem. Soc.* **2021**, *143*, 12025–12037.
- (58) Szabó, C. Hydrogen Sulphide and Its Therapeutic Potential. *Nat. Rev. Drug Discovery* **2007**, *6*, 917–935.
- (59) Sen, N.; Paul, B. D.; Gadalla, M. M.; Mustafa, A. K.; Sen, T.; Xu, R.; Kim, S.; Snyder, S. H. Hydrogen Sulfide-Linked Sulfhydration of NF- κ B Mediates Its Antiapoptotic Actions. *Mol. Cell* **2012**, *45*, 13–24.
- (60) Szabó, C.; Ischiropoulos, H.; Radi, R. Peroxynitrite: Biochemistry, Pathophysiology and Development of Therapeutics. *Nat. Rev. Drug Discovery* **2007**, *6*, 662–680.
- (61) Liu, F.; Liu, G. J.; Liu, N.; Zhang, G.; Zhang, J. X.; Li, L. F. Effect of Hydrogen Sulfide on Inflammatory Cytokines in Acute Myocardial Ischemia Injury in Rats. *Exp. Ther. Med.* **2015**, *9*, 1068–1074.
- (62) Cheng, E. H. Y. A.; Wei, M. C.; Weiler, S.; Flavell, R. A.; Mak, T. W.; Lindsten, T.; Korsmeyer, S. J. BCL-2, BCL-XL Sequester BH3 Domain-Only Molecules Preventing BAX- and BAK-Mediated Mitochondrial Apoptosis. *Mol. Cell* **2001**, *8*, 705–711.
- (63) Chen, Z.; Chua, C. C.; Ho, Y.-S.; Hamdy, R. C.; Chua, B. H. L. Overexpression of Bcl-2 Attenuates Apoptosis and Protects Against Myocardial I/R Injury in Transgenic Mice. *Am. J. Physiol.-Heart C* **2001**, *280*, H2313–H2320.
- (64) Hou, X.; Huang, M.; Zeng, X.; Zhang, Y.; Sun, A.; Wu, Q.; Zhu, L.; Zhao, H.; Liao, Y. The Role of TRPC6 in Renal Ischemia/Reperfusion and Cellular Hypoxia/Reoxygenation Injuries. *Front. Mol. Biosci.* **2021**, *8*, 698975.
- (65) Borrelli, M. A.; Turnquist, H. R.; Little, S. R. Biologics and Their Delivery Systems: Trends in Myocardial Infarction. *Adv. Drug Deliver. Rev.* **2021**, *173*, 181–215.
- (66) Puhakka, M.; Magga, J.; Hietakorpi, S.; Penttilä, I.; Uusimaa, P.; Risteli, J.; Peuhkurinen, K. Interleukin-6 and Tumor Necrosis Factor Alpha in Relation to Myocardial Infarct Size and Collagen Formation. *J. Card. Fail.* **2003**, *9*, 325–332.
- (67) Frangogiannis, N. G.; Smith, C. W.; Entman, M. L. The Inflammatory Response in Myocardial Infarction. *Cardiovasc. Res.* **2002**, *53*, 31–47.
- (68) Choe, G.; Kim, S.-W.; Park, J.; Park, J.; Kim, S.; Kim, Y. S.; Ahn, Y.; Jung, D.-W.; Williams, D. R.; Lee, J. Y. Anti-Oxidant Activity Reinforced Reduced Graphene Oxide/Alginate Microgels: Mesenchymal Stem Cell Encapsulation and Regeneration of Infarcted Hearts. *Biomaterials* **2019**, *225*, 119513.
- (69) Li, L.; Wang, Y.; Guo, R.; Li, S.; Ni, J.; Gao, S.; Gao, X.; Mao, J.; Zhu, Y.; Wu, P.; Wang, H.; Kong, D.; Zhang, H.; Zhu, M.; Fan, G. Ginsenoside Rg3-loaded, Reactive Oxygen Species-Responsive Polymeric Nanoparticles for Alleviating Myocardial Ischemia-Reperfusion Injury. *J. Controlled Release* **2020**, *317*, 259–272.
- (70) Zhang, Y.; Khalique, A.; Du, X.; Gao, Z.; Wu, J.; Zhang, X.; Zhang, R.; Sun, Z.; Liu, Q.; Xu, Z.; Midgley, A. C.; Wang, L.; Yan, X.; Zhuang, J.; Kong, D.; Huang, X. Biomimetic Design of Mitochondria-Targeted Hybrid Nanozymes as Superoxide Scavengers. *Adv. Mater.* **2021**, *33*, 2006570.
- (71) Fujiwara, M.; Matoba, T.; Koga, J.-I.; Okahara, A.; Funamoto, D.; Nakano, K.; Tsutsui, H.; Egashira, K. Nanoparticle Incorporating Toll-like Receptor 4 Inhibitor Attenuates Myocardial Ischaemia-Reperfusion Injury by Inhibiting Monocyte-Mediated Inflammation in Mice. *Cardiovasc. Res.* **2019**, *115*, 1244–1255.
- (72) Zhang, C. X.; Cheng, Y.; Liu, D. Z.; Liu, M.; Cui, H.; Zhang, B. L.; Mei, Q. B.; Zhou, S. Y. Mitochondria-Targeted Cyclosporin A Delivery System to Treat Myocardial Ischemia Reperfusion Injury of Rats. *J. Nanobiotechnol.* **2019**, *17*, 18.
- (73) Che, J.; Najer, A.; Blakney, A. K.; McKay, P. F.; Bellahcene, M.; Winter, C. W.; Sintou, A.; Tang, J.; Keane, T. J.; Schneider, M. D.; Shattock, R. J.; Sattler, S.; Stevens, M. M. Neutrophils Enable Local and Non-Invasive Liposome Delivery to Inflamed Skeletal Muscle and Ischemic Heart. *Adv. Mater.* **2020**, *32*, 2003598.
- (74) Clemons, T. D.; Viola, H. M.; House, M. J.; Iyer, K. S.; Hool, L. C. Examining Efficacy of “TAT-less” Delivery of a Peptide against the L-Type Calcium Channel in Cardiac Ischemia-Reperfusion Injury. *ACS Nano* **2013**, *7*, 2212–2220.
- (75) Paige, A. G.; Whitcomb, K. L.; Liu, J.; Kinstler, O. Prolonged Circulation of Recombinant Human Granulocyte-Colony Stimulating Factor by Covalent Linkage to Albumin Through a Heterobifunctional Polyethylene Glycol. *Pharm. Res.* **1995**, *12*, 1883–1888.
- (76) Yuan, W.; Liu, Z. Surgical Wound Healing Using Hemostatic Gauze Scaffold Loaded with Nanoparticles Containing Sustained-Release Granulocyte Colony-Stimulating Factor. *Int. J. Nanomedicine* **2011**, *6*, 3139–3149.
- (77) Kryza, D.; De Crozals, G.; Mathe, D.; Taleb Sidi-Boumedine, J.; Janier, M.; Chaix, C.; Dumontet, C. Granulocyte-Colony Stimulating Factor Nanocarriers for Stimulation of the Immune System (Part II):

Dose-Dependent Biodistribution and *In Vivo* Antitumor Efficacy in Combination with Rituximab. *Bioconjugate Chem.* **2018**, *29*, 804–812.

(78) Wu, F.; Zhou, Z.; Su, J.; Wei, L.; Yuan, W.; Jin, T. Development of Dextran Nanoparticles for Stabilizing Delicate Proteins. *Nanoscale Res. Lett.* **2013**, *8*, 197.

(79) Napoli, C.; Paolisso, G.; Casamassimi, A.; Al-Omran, M.; Barbieri, M.; Sommese, L.; Infante, T.; Ignarro, L. J. Effects of Nitric Oxide on Cell Proliferation. *J. Am. Coll. Cardiol.* **2013**, *62*, 89–95.

(80) Yang, T.; Zelikin, A. N.; Chandrawati, R. Progress and Promise of Nitric Oxide-Releasing Platforms. *Adv. Sci.* **2018**, *5*, 1701043.

(81) Coneski, P. N.; Schoenfisch, M. H. Nitric oxide release: Part III. Measurement and Reporting. *Chem. Soc. Rev.* **2012**, *41*, 3753–3758.

(82) Thomas, D. D.; Ridnour, L. A.; Isenberg, J. S.; Flores-Santana, W.; Switzer, C. H.; Donzelli, S.; Hussain, P.; Vecoli, C.; Paolucci, N.; Ambs, S.; Colton, C. A.; Harris, C. C.; Roberts, D. D.; Wink, D. A. The Chemical Biology of Nitric Oxide: Implications in Cellular Signaling. *Free Radical Bio. Med.* **2008**, *45*, 18–31.

(83) Liu, S.; Li, W.; Chen, H.; Zhou, J.; Dong, S.; Zang, P.; Tian, B.; Ding, H.; Gai, S.; Yang, P.; Zhao, Y. On-Demand Generation of Peroxynitrite from an Integrated Two-Dimensional System for Enhanced Tumor Therapy. *ACS Nano* **2022**, *16*, 8939–8953.

Recommended by ACS

Transforming Cancer-Associated Fibroblast Barrier into Drug Depots to Boost Chemo-Immunotherapy in “Shooting Fish in a Barrel” Pattern

Shijun Yuan, Na Zhang, *et al.*

JUNE 16, 2023

ACS NANO

READ 

Biomimetic Nanoparticle-Mediated Target Delivery of Hypoxia-Responsive Plasmid of Angiotensin-Converting Enzyme 2 to Reverse Hypoxic Pulmonary Hypertension

Rui Yuan, Mingqing Dong, *et al.*

APRIL 18, 2023

ACS NANO

READ 

Reversal of HMGA1-Mediated Immunosuppression Synergizes with Immunogenic Magnetothermodynamic for Improved Hepatocellular Carcinoma Therapy

Bin Yan, Xiaoli Liu, *et al.*

MAY 10, 2023

ACS NANO

READ 

Enhanced Local Delivery of microRNA-145a-5P into Mouse Aorta via Ultrasound-Targeted Microbubble Destruction Inhibits Atherosclerotic Plaque Formation

Yu Wu, Mingxing Xie, *et al.*

JANUARY 19, 2023

MOLECULAR PHARMACEUTICS

READ 

Get More Suggestions >